

# SPECTRAL DOMAIN OPTICAL COHERENCE TOMOGRAPHY FOR GLAUCOMA (AN AOS THESIS)

---

BY Joel S. Schuman MD FACS

## ABSTRACT

**Purpose:** Optical coherence tomography (OCT) is a rapidly evolving, robust technology that has profoundly changed the practice of ophthalmology. Spectral domain OCT (SD-OCT) increases axial resolution 2- to 3-fold and scan speed 60- to 110-fold vs time domain OCT (TD-OCT). SD-OCT enables novel scanning, denser sampling, and 3-dimensional imaging. This thesis tests my hypothesis that SD-OCT improves reproducibility, sensitivity, and specificity for glaucoma detection.

**Methods:** OCT progress is reviewed from invention onward, and future development is discussed. To test the hypothesis, TD-OCT and SD-OCT reproducibility and glaucoma discrimination are evaluated. Forty-one eyes of 21 subjects (SD-OCT) and 21 eyes of 21 subjects (TD-OCT) are studied to test retinal nerve fiber layer (RNFL) thickness measurement reproducibility. Forty eyes of 20 subjects (SD-OCT) and 21 eyes of 21 subjects (TD-OCT) are investigated to test macular parameter reproducibility. For both TD-OCT and SD-OCT, 83 eyes of 83 subjects are assessed to evaluate RNFL thickness and 74 eyes of 74 subjects to evaluate macular glaucoma discrimination.

**Results:** Compared to conventional TD-OCT, SD-OCT had statistically significantly better reproducibility in most sectoral macular thickness and peripapillary RNFL sectoral measurements. There was no statistically significant difference in overall mean macular or RNFL reproducibility, or between TD-OCT and SD-OCT glaucoma discrimination. Surprisingly, TD-OCT macular RNFL thickness showed glaucoma discrimination superior to SD-OCT.

**Conclusions:** At its current development state, SD-OCT shows better reproducibility than TD-OCT, but glaucoma discrimination is similar for TD-OCT and SD-OCT. Technological improvements are likely to enhance SD-OCT reproducibility, sensitivity, specificity, and utility, but these will require additional development.

*Trans Am Ophthalmol Soc 2008;106:426-458*

## INTRODUCTION

---

Imaging of the eye has grown significantly in importance for the diagnosis of ocular diseases over the last 20 years. Out of a variety of techniques such as scanning laser polarimetry and confocal scanning laser ophthalmoscopy, optical coherence tomography (OCT) has emerged to the forefront of ocular imaging because of the wide variety of information it can provide, its high resolution, and the complex 3-dimensional (3D) data it is able to gather. Many changes to the technology are still being made, improving axial and transverse resolution of the images and decreasing the time necessary for image acquisition.

Optical coherence tomography is a method of using low-coherence interferometry to determine the echo time delay and magnitude of backscattered light reflected off an object of interest. This method can be used to scan through the layers of a structured tissue sample such as the retina with very high axial resolution (3 to 15  $\mu\text{m}$ ),<sup>1-10</sup> providing images demonstrating 3D structure. Because of the unique optically clear pathway through the eye, OCT has been used most extensively for imaging disorders affecting the retina.<sup>3,6-8,10-31</sup> It has also been used in the anterior segment of the eye<sup>32-35</sup> as well as to view the structure of nonocular tissues, including breast,<sup>36</sup> kidney,<sup>37</sup> and skin lesions,<sup>38-43</sup> among others.

This thesis aims to discuss the history and use of OCT as well as the future of OCT research. To investigate the use of spectral domain OCT (SD-OCT), the most advanced OCT method available commercially for clinical use, a study was performed comparing the reproducibility and glaucoma discriminating ability of SD-OCT to time domain OCT (TD-OCT). A variety of case studies from glaucomatous and healthy eyes is also presented to illustrate the clinical utility and potential value of SD-OCT.

## HISTORY OF OCT

Given how pervasive OCT is in the clinical practice of ophthalmology, it is sobering to realize that the development of ophthalmic OCT began just under 20 years ago. The first retinal imaging was performed in 1989 in the laboratory of James G. Fujimoto, PhD, by David Huang, MD, PhD, then a Harvard Medical School, Cambridge, Massachusetts, and Massachusetts Institute of Technology, Cambridge, Massachusetts, Health Sciences Technology (HST) MD, PhD candidate, and Joel S. Schuman, MD, then a fellow in ophthalmic research and glaucoma at Harvard University and Massachusetts Eye and Ear Infirmary, Boston, Massachusetts. The first prototype ophthalmic OCT was placed at the New England Eye Center, Tufts-New England Medical Center, Tufts University School of Medicine in Boston, Massachusetts, and in vivo ocular imaging of subjects began in 1994. In 1994 the technology was patented and transferred to Carl Zeiss Meditec, Inc (Dublin, California), and the first commercially available OCT, called OCT 1000, was marketed in 1996. The technology went through 2 iterations, resulting in OCT 2000 in the year 2000 and then OCT 3 (Stratus OCT), which became commercially available in 2002. More than 7000 of these units are in clinical use worldwide, and many consider OCT 3 the current "gold standard" for retinal imaging. In 2006, the first high-speed, high-resolution OCTs, known variously as Fourier domain OCT, SD-OCT, or hsHR-OCT (all describing the same technology), became commercially available.

The first demonstrations of OCT were presented by Huang and colleagues<sup>44</sup> in *Science* in 1991; they used a prototype OCT device

From the UPMC Eye Center, Eye and Ear Institute, Ophthalmology and Visual Science Research Center, Department of Ophthalmology, University of Pittsburgh School of Medicine, the Department of Bioengineering, Swanson School of Engineering, University of Pittsburgh, and the Center for the Neural Basis of Cognition, University of Pittsburgh and Carnegie Mellon University, Pittsburgh, Pennsylvania.

to image a human retina and coronary artery *ex vivo*. Images had approximately 15- $\mu\text{m}$  axial resolution, allowing visualization of some of the layered retinal and optic nerve head structure and the composition of the wall of the coronary artery. Huang and colleagues were able to compare OCT images with histology of the same tissue and define the structures that could be seen using this first-generation prototype TD-OCT. Fercher and associates<sup>45</sup> presented the first *in vivo* OCT images in 1993, and the same group of researchers who originally presented OCT in 1991 produced the first images of retinal disease in 1995.<sup>29,30</sup> Images of the retina were presented, with axial resolution improved in the OCT device to 10  $\mu\text{m}$ . The prototype instrument was based on a slit-lamp biomicroscope that was modified to provide a view of the fundus for image alignment and would enable simultaneous OCT imaging. Using this system, they demonstrated imaging of both the foveal contour and optic nerve head *in vivo*.

A major event in the evolution of OCT was the use of light wavelengths instead of time delay to determine the spatial location of reflected light. Through the use of Fourier transformation, this took the technology from the original method of TD-OCT to the development of SD-OCT. The original OCT method, known as TD-OCT, encoded the location of each reflection in the time information relating the position of a moving reference mirror to the location of the reflection.<sup>44,45</sup> SD-OCT, instead, acquires all information in a single axial scan through the tissue simultaneously by evaluating the frequency spectrum of the interference between the reflected light and a stationary reference mirror. This method enables much faster acquisition times, resulting in a large increase in the amount of data that can be obtained during a given scan duration using SD-OCT.<sup>4,9,20,46</sup> More detailed information can be found in the "OCT Techniques" section that follows.

The first SD-OCT *in vivo* scans presented were by Wojtkowski and colleagues in 2001,<sup>47</sup> describing the technical details of the method and math behind it, as well as an *in vivo* scan of a fingernail. The data capture was rapid, but it took 30 minutes to obtain and process the image, making this technology impractical for clinical use at that time. The first SD-OCT ophthalmic scans were presented by the same group the following year, where *in vivo* scans of the iris, lens, macula, and optic disc were all displayed.<sup>20</sup> Processing time was improved so that it took only 20 seconds to obtain and process each 500 $\times$ 500-pixel image. From this early experimental start, SD-OCT devices have been approved for clinical use by the US Food and Drug Administration (FDA) and can now acquire 3D data sets consisting of several hundred scans of 200 $\times$ 200 $\times$ 1024 pixels in 2 seconds. Research prototype nonclinical machines are even faster and have better axial resolution.

At the time of this writing, at least 7 companies manufacture and sell SD-OCT devices: Biotigen, Inc, Research Triangle Park, North Carolina; Carl Zeiss Meditec, Inc, Dublin, California (Cirrus HD-OCT); Heidelberg Engineering GmbH, Heidelberg, Germany (Spectralis OCT); Optopol Technology, SA, Zawiercie, Poland (SOCT Copernicus HR); Optovue, Inc, Fremont, California (RTVue); Ophthalmic Technologies Inc, OTI, Toronto, Ontario (OCT/SLO); and Topcon Medical Systems, Inc, Paramus, New Jersey (3D-OCT 1000).

Optical coherence tomography has been used to a lesser extent beyond retinal imaging. Imaging of the anterior eye was first presented by Izatt and colleagues in 1994.<sup>53</sup> Images were acquired with a light source centered at an 800-nm wavelength, shorter than that typically used for retinal imaging. This system provided an axial resolution of approximately 10  $\mu\text{m}$ , with the shorter wavelength allowing greater detail but less penetration into the anterior chamber angle and posterior to the iris. Current clinical systems for anterior eye imaging, such as the Visante (Carl Zeiss Meditec, Inc, Dublin, California), use light source centered at a wavelength of approximately 1310  $\mu\text{m}$  to allow for penetration into the iris and angle, though at the expense of some resolution.<sup>34,35,48</sup> Optical coherence tomography can be used as an "optical biopsy" to help guide procedures in the eye and beyond. This is most valuable where traditional excisional biopsy is dangerous, such as in the coronary arteries, retina, and other neural tissues.<sup>49-53</sup> In the tissues other than the eye, which are not optically transparent, use of endoscopic OCT during minimally invasive surgery allows visualization of the 3D structure of the tissue while checking for plaques or other lesions. In instances where excisional biopsy may have sampling errors, it can be helpful to help guide a biopsy so tumor tissue is not missed. Optical coherence tomography provides visualization directly and in real time, allowing it to guide microsurgical procedures minimally invasively.

In addition to observation of the structure of the retina and other tissues, OCT has begun to be used for monitoring the function of tissue characteristics. Retinal blood flow studies are in their initial stages, using Doppler OCT methods similar to Doppler ultrasound to look at flow both quantitatively and qualitatively.<sup>54-57</sup> Kagemann and colleagues<sup>58</sup> used the spectral data of SD-OCT to assess blood oxygenation in retinal arteries and veins. Three studies have been published demonstrating "optophysiology," in which OCT was used to identify changes in the reflectance of certain layers of the *in vivo* retina following exposure to light, providing the foundation for future functional OCT studies.<sup>59-61</sup>

Optical coherence tomography technology has improved substantially over a relatively short period of time, from TD-OCT to the higher-speed, higher-resolution SD-OCT, to new image processing and analysis techniques that allow researchers to identify tissue properties beyond structure. The history of the OCT technology demonstrates the rapid expansion of the field of OCT, with new research appearing continuously: Published articles on OCT have risen from less than 5 per year from 1991 to 1994 to nearly 1000 in MEDLINE in 2006 alone.

## OCT TECHNIQUES

To best see where OCT is headed, the present instrumentation for acquiring images should be understood from a basic technical perspective. TD-OCT will be presented first, as SD-OCT uses similar hardware with a few modifications.

TD-OCT is frequently compared to ultrasound, because their basic principles are analogous, with OCT using light as its medium, whereas ultrasound uses sound. Both methods create a cross-sectional image by measuring the echo time delay and intensity of the reflected and backscattered light or sound. OCT images use this information to depict variations in optical reflectance through the

depth of the tissue along a point, creating what is known as an A-scan. These single axial scans through the tissue can be gathered linearly across the tissue, making one cross-sectional image, known as a B-scan, and a collection of parallel B-scans can be used to gather a 3D data set. Because of the difference in medium, OCT has a much higher axial resolution than ultrasound,  $\sim 10 \mu\text{m}$  for TD-OCT<sup>1,5,6</sup> and  $\sim 5$  to  $7 \mu\text{m}$  for SD-OCT<sup>7-10</sup> vs  $\sim 150 \mu\text{m}$  for ultrasound at a frequency of 10 MHz. Higher axial resolutions can be achieved with higher frequencies of ultrasound. Ultrasound at 50 to 80 MHz has axial resolutions of  $\sim 50$  to  $20 \mu\text{m}$ , but with a penetration depth of only 4 to 3 mm.<sup>62</sup> The use of light as the medium in OCT gives it the advantage of being noncontact for the patient, whereas ultrasound needs a coupling medium such as water along its path between transmitter and tissue to pass the sound waves. These physical differences make ultrasound useful for measuring intraocular distances and overall structure of the anterior eye, with greater penetration of signal into the angle where near-infrared light is blocked by the sclera, but OCT is far more useful for detecting detailed structures in the retina and anterior segment.

While the general principle of using reflections to create the images is the same for OCT and ultrasound, the methods for detecting these reflections are not. Because light is so much faster than sound, the time delays between reflections from different layers cannot be measured directly, since differences would be on the order of femtoseconds. Optical coherence tomography uses low-coherence interferometry to see the time difference corresponding to the distances between structures.<sup>44</sup> The process starts with a broadband laser or superluminescent diode low-coherence light source, the beam from which travels to a beam splitter. One half of the light goes to a mirror at a known position on a reference arm, and the other goes to the sample arm, where it is scattered and reflects off of tissue structures. Light from the reference and sample arms travels back to the beam splitter and recombines to form an interference pattern, which is sensed by a photodetector. The light beams combine constructively only if the light from the tissue and the light from the reference mirror are at almost exactly the same distance. The width of the signal envelope defines the resolution of the interferometer and is determined by the coherence length of the light used; the shorter the coherence length, the finer the resolution. The coherence length is dependent on the bandwidth, with broader bandwidths producing lower-coherence light. In TD-OCT, for each axial scan, the position of the reference mirror is oscillated to allow imaging of a known range of depths in the tissue. Each pixel in the A-scan represents the intensity of the reflection at that position. This intensity is converted to a log scale because of the approximately 45-dB-wide variation in intensity. The original design of the OCT system was based on a Michelson interferometer optical setup (Figure 1, MI). A schematic of a current fiber-optics-based TD-OCT system is shown in Figure 1, TD-OCT.

SD-OCT is similar in principle; however, the signal acquisition varies slightly, but importantly, from TD-OCT. Instead of a moving reference mirror, the mirror is stationary, and the interference pattern is split by a grating into its frequency components and all of these components are simultaneously detected by a charge-coupled device (CCD). The CCD has an array of photodetectors, each sensitive to a range of specific frequencies.<sup>4,9,20,46</sup> Each frequency detected corresponds to a certain depth within the tissue after Fourier transform of the received signal, allowing all points along each A-scan to be gathered simultaneously, greatly accelerating scan speed. These A-scans can then be acquired along a transverse plane through the tissue and assembled into B-scans, as is done with TD-OCT. SD-OCT is also known as Fourier domain OCT because the distances are encoded in the Fourier transform of the frequencies of light reflected. Figure 1, SD-OCT, presents a schematic of an SD-OCT system.

The primary disadvantages of TD-OCT compared to SD-OCT are the moving mirror on the reference arm and resultant slower acquisition speed. As already stated, axial resolution along each A-scan depends on the properties of the light source used, particularly its coherence length defined by its full width at half maximum.<sup>9</sup> Transverse resolution is dependent on the beam waist size.<sup>26</sup> This is defined fundamentally by the optics projecting the beam as well as any aberrations in the eye. Scan density is sometimes incorrectly interpreted as transverse resolution and is dependent on A-scan sampling rate. Current typical TD-OCT B-scans have an axial resolution of  $\sim 10 \mu\text{m}$ , with 128 or 512 A-scans comprising an image 4 to 6 mm wide transversely, with transverse resolution of 20 to  $25 \mu\text{m}$ , and a scan speed of 400 A-scans per second.<sup>6,44,45,63</sup> As the number of A-scans increases, the scan time increases. Therefore, on a TD-OCT machine, there is a trade-off between long- and short-duration scans; a long-duration scan may provide better scan density, giving the appearance of better transverse resolution, since there are more scans and therefore more detail. On the other hand, the more A-scans acquired, the longer the scan time and the higher the likelihood of eye motion-induced artifact. Shorter-duration scans have lower transverse scan densities but are less susceptible to motion artifact.

Because even commercially available SD-OCT devices are 40 to 110 times faster than TD-OCT, they are able to acquire data extremely quickly. For example, at 16,000 A-scans per second, SD-OCT can acquire a B-scan image containing 2048 A-scans in 0.13 seconds, and at 55,000 A-scans per second (eg, Copernicus, Optopol Technology, SA), the same OCT would require less than 0.04 second<sup>7,8,10</sup>; TD-OCT captures 512 A-scans in 1.3 seconds.<sup>6,44,45,63</sup> This faster speed allows for 3D data sets to be gathered, composed of a series of rapidly acquired B-scans. These 3D data sets may be subject to motion artifacts in between B-scans, but as OCT technology improves, there is less movement artifact, since scanning time is shorter. With the 3D data sets, we can use 3D rendering, modeling, and manipulation tools to allow more intuitive visualization of the structure in the data set, similar to the 3D visualization tools created for magnetic resonance imaging or computed tomographic scans. Many of these tools will require additional technology development for realization.

Both B-scans and 3D data sets have a variety of computer processing techniques that can be used to improve images or from which quantitative data can be gleaned. The images can be represented as either grayscale or false color images. Grayscale gives a more intuitive interpretation and may make small details more visible. However, the computer can only prove 8 bit (256 level) gray resolution, and the observer's eye is limited in the number of levels of gray it can distinguish. Color can be displayed at 24 bit or more, and the eye has a much easier time differentiating millions of colors. Because of this, OCT displays often use false color images to improve the ability to differentiate tissue structures, although the colors may induce artifacts. A typical color map sets red and white at

the highest intensity level of  $\sim -50$  dB, and blue and black at the lowest intensity of  $\sim -95$  dB.

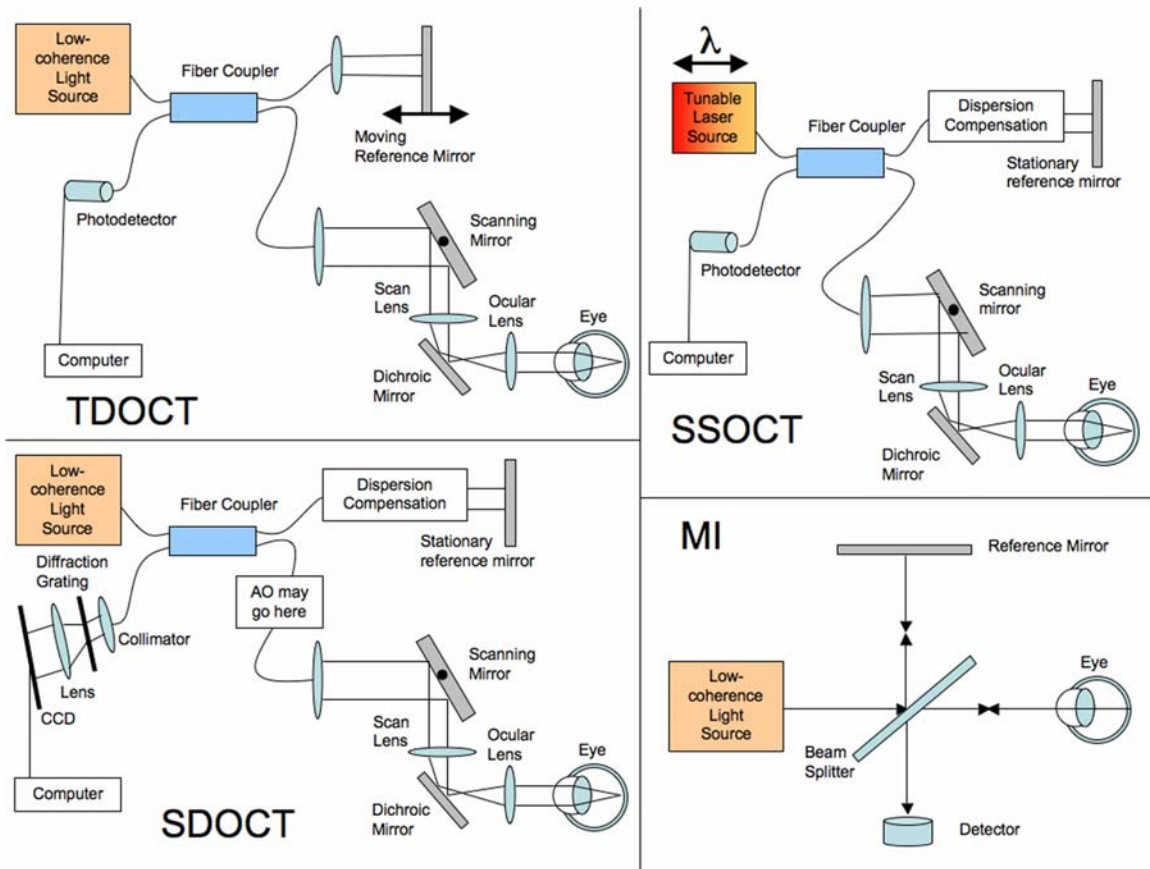


**FIGURE 1**

Optical coherence tomography (OCT) schematics: time-domain OCT (TD-OCT), spectral-domain OCT (SD-OCT), swept-source OCT (SS-OCT), and the adaptive optics system that can be added into a SD-OCT system (AO-OCT). Light signals are split and exchanged through the fiber coupler. The scanning mirror scans the beam across to make a B-scan. The dispersion correction of SD-OCT and SS-OCT corrects for light dispersion through the length of the eye and can be done through software after acquisition or through a material like a cuvette of distilled water approximately the length of the eye to compensate. The collimator in SD-OCT collects the light to shine it through a diffraction grating that spreads the different frequencies of light across the charge-coupled device (CCD) camera.

Overall scan averaging and eye motion correction can also improve image quality. Adjacent pixels or A-scans can be averaged or dithered to reduce noise and improve signal within a B-scan, or adjacent B-scans can be averaged to improve the signal-to-noise ratio within a 3D SD-OCT data set. These signal-to-noise improvement techniques are similar to those used in many fields, including electrophysiology.

Image registration can be used to correct motion artifact in a given SD-OCT scan, through alignment of multiple B-scans based on tissue structural features.<sup>64</sup> Because 3D data sets can be acquired, the 3D data cube can be presented with all pixels in each given A-scan summed, producing an OCT fundus image. Not surprisingly, the OCT fundus image resembles a photograph, which also axially sums reflections from all tissue layers. The OCT fundus image can be used for image alignment or registration based on tissue features, such as blood vessel continuities or discontinuities. The 3D OCT can also be aligned or registered to an SLO image or a fundus photograph acquired simultaneously or nearly so. Use of the OCT fundus image has the advantage in that it is composed of the actual OCT topographic data; however, the SLO or fundus photograph has the advantage of faster acquisition and minimal movement artifact. These techniques are not mutually exclusive, and some or all may be used. Combining techniques may offer the advantages of using both the actual OCT data and rapid image acquisition.

Three-dimensional OCT data cubes can be registered from visit to visit, and the data sets can be arbitrarily resampled post hoc, allowing measurement of exactly the same tissue areas from visit to visit or scan to scan. This would be expected to reduce

measurement variability and enhance sensitivity and specificity for detection of disease progression. Unfortunately, at the time of this writing, alignment and registration of data within individual 3D OCT data cubes are still in the process of development, and registration of 3D data cubes from scan to scan and visit to visit remains a goal and is not yet a reality.

Image analysis using automated segmentation techniques is vital for extracting quantitative values that can be used to measure tissue layers in order to detect structural damage and track disease progression. OCT images can be processed with intelligent algorithms to extract features like retinal thickness in the macula and retinal nerve fiber layer (RNFL) thickness around the optic nerve head. Image processing algorithms can identify both superficial boundaries, like the vitreoretinal interface, and boundaries of the inner retinal layers, such as the retinal pigment epithelium (RPE) or plexiform layers.<sup>21,65,66</sup> Eventually, it should be possible to segment each tissue layer in the retina, cornea, or other ocular structures. At present, it is possible to segment the total retinal thickness, RNFL, and to automatically identify and measure the “inner retinal complex,” consisting of the RNFL, retinal ganglion cell layer (RGCL), and inner plexiform layer. Segmentation steps often include smoothing, edge detection, and error correction. Using these algorithms may not be anatomically precise, with the most easily detectable reflectance differences in retinal layers not necessarily corresponding exactly to structural layers, but measurement is often robust and repeatable, which is valuable for examining changes in a patient over time, even if not an absolute measure of a specific histologic anatomic feature.

Once a normative database is developed and deployed for a particular scan type, segmentation algorithms can be applied to it, providing a range of thickness measurements classified as normal, based on other, more classic ophthalmologic findings and tests, such as perimetry. Patients’ scans can then be compared against this normative database, to determine whether their tissue structures are within the healthy range or would be considered borderline or outside normal limits.

Once again, current image analysis techniques require additional development in order to take advantage of the rich data and powerful potential of SD-OCT imaging. At present, we are limited to total retinal thickness and RNFL segmentation on many SD-OCT devices, although some do not even have any segmentation software available at the time of this writing. Normative databases are in the process of being collected, vetted, and implemented for several of the commercial OCT devices, but none have been deployed as of the time of this manuscript preparation. The ability to measure the actual tissue cellular layer or layers affected by a given disease process, and to compare these measurements to healthy eyes in the population, is likely to greatly enhance our ability to detect disease and its progression.

Segmentation is especially important in the case of glaucoma. The most commonly used TD-OCT scan type for assessment of glaucoma is a 3.4-mm-diameter circumpapillary scan centered on the optic nerve head. Segmentation algorithms allow measurement of the thickness of the RNFL, which appears as the highly backscattering “red” layer at the vitreoretinal interface. RNFL thickness is highly correlated with glaucomatous damage, and RNFL thinning is often one of the first signs of the disease, frequently measurable even before visual field changes can be detected.<sup>10,29,67</sup> Segmentation and measurement of this layer are important in that it is a more sensitive and specific discriminator of glaucomatous damage than measurement of the entire retinal thickness. On the other hand, when Schuman and colleagues<sup>68</sup> defined the 3.4-mm circumpapillary RNFL thickness scan as the standard for TD-OCT glaucoma assessment, that scan was the best that could be done with the available technology at that time. It may be that other measurement parameters will have greater discriminating or progression detection abilities using SD-OCT, especially with normative cross-sectional and longitudinal data, 3D scanning, and, in particular, with 3D image alignment and registration. This remains to be investigated and will require improvements in image analysis abilities to evaluate.

## **OCT IN GLAUCOMA**

Optical coherence tomography is of particular utility in glaucoma, since it provides high-resolution objective, quantitative assessment of the retinal cellular layers affected by the disease. Especially because glaucoma is a disease defined by clinical appearance of the optic nerve and visual field, objective and quantitative measures could potentially provide a more accurate and precise method for the diagnosis of glaucoma and detection of its progression. Clinical optic disc changes include characteristic diffuse or focal narrowing or notching of the optic nerve neuroretinal rim, in particular at the inferior or superior poles; diffuse or localized abnormalities of the RNFL, mainly superior-temporally or inferior-temporally; optic nerve head hemorrhages; and asymmetric appearance of the optic disc rim between fellow eyes, suggesting loss of neural tissue in one (although this last parameter is the weakest by far, since asymmetric cupping is more often due to asymmetric disc size than to disease).<sup>69,70</sup> Chronic progressive loss of neural tissue is a hallmark of the disease and has been suggested as the criterion for the diagnosis of glaucoma in clinical studies of the disease.<sup>71</sup> Typical perimetric abnormalities associated with glaucoma are a nasal step or scotoma, inferior or superior arcuate scotomas, paracentral scotoma, generalized depression across the field, and, most important, progressive deterioration of the visual field.<sup>72</sup> The risk factors most strongly associated with the development and severity of glaucoma include high intraocular pressure (IOP), low central corneal thickness, family history of glaucoma, black African descent, advanced age, myopia, hyperopia, Asian or Inuit descent, cardiovascular disease, vasculopathy, and diabetes.<sup>73-75</sup> Glaucoma results in (usually) gradual loss of retinal ganglion cells and their projections<sup>76,77</sup> related to deformation and abnormalities in the lamina cribrosa and is often associated with transsynaptic degeneration in the lateral geniculate nucleus and beyond as well.<sup>78-82</sup>

Past OCT research in glaucoma has primarily focused on TD-OCT, particularly on the 3.4-mm-diameter circumpapillary scans using OCT 3 and prior OCT iterations (Carl Zeiss Meditec, Inc, Dublin, California).<sup>31,83-86</sup> Retinal nerve fiber layer thickness profiles created by retinal segmentation have been compared to normative data as well as evaluated over time to track disease progression.<sup>86</sup> Reproducibility has been found to be reasonable, with a standard deviation of measures of ~2.5  $\mu\text{m}$  for mean overall RNFL thickness from visit to visit, and can be improved if subjects are dilated for their scans.<sup>84,87</sup> Axial resolution of ~10  $\mu\text{m}$ , while not fine enough to

see the degree of retinal laminar definition observed with ultrahigh resolution OCT (~2 to 3  $\mu\text{m}$ ) imaging, is typically sufficient to establish a reliable measurement of RNFL thickness. Segmentation algorithms must be checked with each scan, as they can fail on account of poor scan quality.<sup>88,89</sup>

There are many potential advantages that SD-OCT may provide for glaucoma detection and follow-up as this technology develops. The higher resolution, currently at 5 to 7  $\mu\text{m}$  commercially, and with research systems at 2 to 3  $\mu\text{m}$ , can provide images of subtle abnormalities or progression currently not visible with TD-OCT and would potentially allow improved segmentation and greater accuracy in measurements of retinal layers.<sup>8</sup> The faster capture times allow the creation of 3D data sets. Since there is much denser sampling and imaging of a broader area, better visualization of RNFL or RGCL defects is possible within the 3D data set, and the 3D data cube has much less interpolation between adjacent points than the sparser TD-OCT scans. Three-dimensional SD-OCT imaging should improve reproducibility, sensitivity, and specificity in the detection of disease and its progression; however, this will require additional technology development, especially with regard to image processing and image analysis.

SD-OCT also provides the potential to gather retinal functional data that could be associated with glaucoma. For example, Doppler OCT could be used to visualize and measure retinal blood flow, and specific frequencies from the spectral data can provide information about blood oxygenation in retinal vessels, as has already been demonstrated, but is currently a labor-intensive research endeavor.<sup>54-58</sup> Better understanding of retinal blood flow could act as a gauge of the health of the retinal tissue. Optophysiology may allow functional glaucoma assessment, through objective, quantitative measurements of changes in reflectance of retinal tissue when exposed to light.<sup>59-61</sup> The use of SD-OCT to measure retinal function is still in the very early stages of development, but as the technology matures, SD-OCT may be used to provide heretofore difficult-to-realize or even unobtainable clinically relevant information beyond retinal structure.

### FUTURE DIRECTIONS FOR OCT

There is a promising future for the growth of SD-OCT in the clinical realm. Gathering data for normative databases for the various commercial SD-OCT devices is already under way at the time of this writing, and the logical extension of this is that software should soon be available that can provide comparisons between a given patient's ocular structure and that of the healthy population of a similar age, gender, and ethnicity.

Progress in research uses of SD-OCT is also a major direction for the future. There is a tremendous amount of knowledge that can be gained from OCT imaging beyond the basic structural information that OCT has been used to provide to date. Doppler OCT for the investigation of optic nerve and retinal blood flow is possible even with TD-OCT, but is greatly enhanced by the rapid data acquisition feasible with SD-OCT.<sup>54-57</sup> Progress is being made toward measurement of other ocular flow parameters, such as measurement of blood flow in scleral vessels or aqueous flow in Schlemm's canal and collector channels (J. S. Schuman, MD, unpublished data, 2007). Understanding of the oxygen content within these vessels may also lead to a better understanding of the vascular and metabolic components of glaucoma and other diseases. The near-infrared wavelengths of light used in SD-OCT may be useful for spectroscopy and oximetry in examining tissue and cellular biochemistry.<sup>58,90</sup>

SD-OCT may also be helpful for the study of disease processes in animal models, especially in small animals. Rodent models of ocular disease are very common and well established, and SD-OCT may be a valuable technology for examination of these models cross-sectionally and longitudinally, reducing the need for sacrifice and allowing observation of the same animal at various time points, rather than having to sacrifice multiple animals at different time points for histology.<sup>91,92</sup> Additionally, zebrafish embryos and adults are increasingly valuable and common genetic models. The high resolution of SD-OCT may allow visualization of the internal structures of the embryos, including the developing eyes, as early as 24 hours postfertilization. Embryos can be re-imaged at various time points, creating a longitudinal data set not available when using histology. Imaging using SD-OCT is noninvasive, so embryonic development proceeds normally after images are acquired (J. S. Schuman, MD, unpublished data, 2007).

While SD-OCT is the current commercially available state-of-the-art, development of new OCT technologies to improve acquisition speed and transverse resolution of images are also under investigation. A new method that affords much higher acquisition speeds is swept-source OCT (SS-OCT).<sup>27,28,61,93</sup> It is another Fourier domain technique for OCT; however, it differs from SD-OCT in the method used to rapidly acquire data. SD-OCT uses a broad-bandwidth light source to provide light at a wide range of wavelengths simultaneously. A CCD as described above captures the reflection of this. The acquisition speed of the signal is limited by this CCD array, and spectrometer resolution limits can result in image drop-off, depending on imaging depth, resulting in a reduction in both resolution and sensitivity with increasing depth in the scan window. SS-OCT instead uses a single tunable laser source that very quickly scans through the range of relevant frequencies. The reflectance of this tuned beam can then be detected by a single photodetector, which is much faster than a CCD array and is also much less expensive and complex than the CCD photodetector array.<sup>27,28,94,95</sup> Figure 1 SS-OCT presents a schematic of a SS-OCT system. SS-OCT is able to acquire images at more than 210,000 A-scans per second, resulting in much faster acquisition times than with TD-OCT or SD-OCT.<sup>27,28,94,95</sup> Because of this, imaging can have a much higher scan density, with transverse oversampling resulting in effectively improved transverse resolution in the data set. This could be very relevant to visualizing fine transverse details such as axons, blood vessels, or perhaps individual retinal cells. High transverse scan density also allows for greater scan averaging for signal-to-noise ratio improvement. Currently, SS-OCT axial resolution is limited to ~10  $\mu\text{m}$  by the abilities of the tunable lasers within wavelengths bounded by water absorption peaks,<sup>27,28,94,95</sup> but as laser technology improves, the potential for broad-bandwidth tunable lasers exploitable for SS-OCT in wavelengths other than those currently available will enable high or ultrahigh axial resolution in addition to ultrafast scan speeds.

In the eye, the ultrafast high-density transverse scanning possible with SS-OCT can provide some improvement in effective

transverse resolution; however, this improvement is limited by aberrations in the optical path through the ocular lens and cornea. This can be corrected for by adding adaptive optics to the OCT system. Adaptive optics is the use of deformable mirrors to determine and correct for these aberrations, increasing transverse resolution to less than  $1\ \mu\text{m}$ .<sup>26,96-100</sup> An adaptive optics system is presented in Figure 2. Adaptive optics has been used more extensively in the eye in scanning laser ophthalmoscopy and fundus photography<sup>98-101</sup> but recently has been incorporated into OCT (AO-OCT) in some research laboratories, because it has the potential to provide the best combination of axial and transverse resolution.<sup>96,97</sup> On the downside, adaptive optics does restrict the overall field of view substantially, allowing the extremely fine focus in only a very small area of the retina. It is likely that future use of AO-OCT will focus on using SD-OCT or SS-OCT for a high-resolution broad view of the retina, with AO-OCT used to hone in on the cellular structures in the area of particular interest.

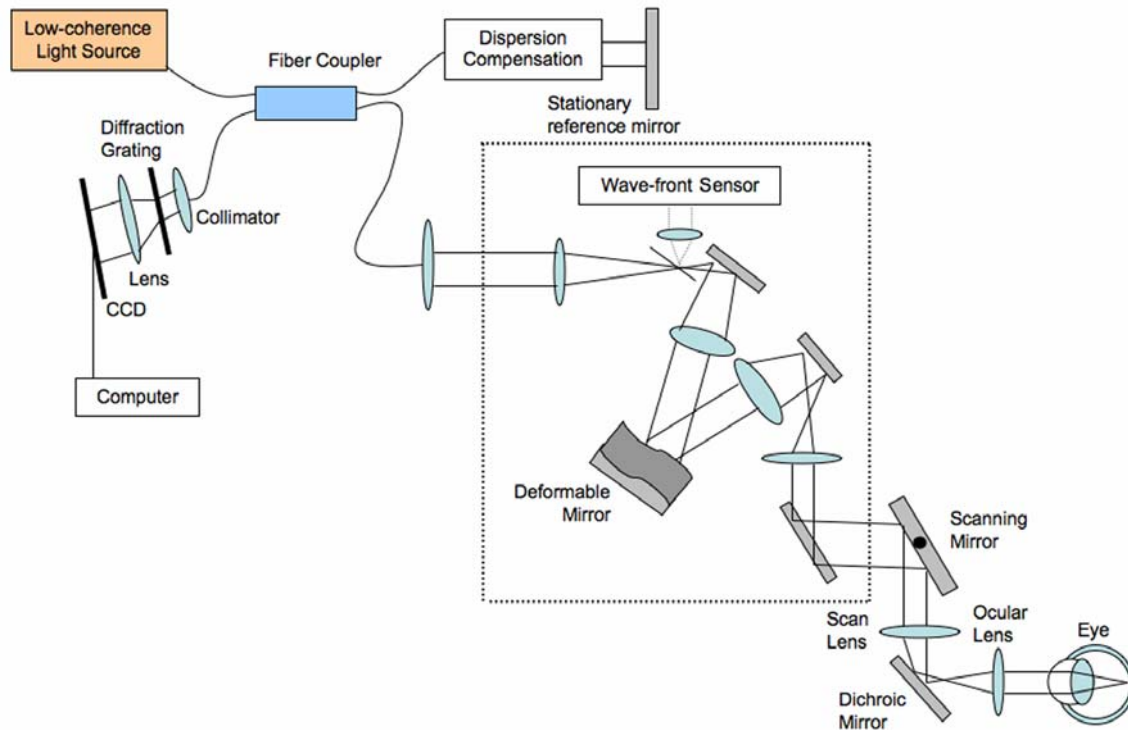


**FIGURE 2**

Spectral domain optical coherence tomography with adaptive optics schematics: The adaptive optics portion of the system is in the dotted box. The wavefront sensor in the adaptive optics system detects the aberrations occurring in the light and sends this information in a feedback loop to the deformable mirror (connection not shown).

Optical coherence tomography has an amazingly short history within ophthalmology relative to its impact on the field. In that brief time there has been substantial growth in the technology, from TD-OCT to SD-OCT, to new developments in image processing and image analysis, to SS-OCT and AO-OCT. The applications of OCT within ophthalmology are wide-reaching, from clinical care to research in the human eye, to animal research in various disease models. Much of the pioneering research and current research has focused on the use of OCT in glaucoma and other retinal diseases. It is in glaucoma where OCT can be particularly valuable for detecting slight RNFL, macular, or optic nerve head abnormalities and for monitoring the slow progression of the disease for subtle changes.

While it is clear that this is a rapidly evolving technology and that we are not even close to exploiting the full power and scope of OCT, this research thesis focuses on establishing the reproducibility and glaucoma discrimination abilities of SD-OCT with state-of-the-art segmentation software of our own design.

#### **PURPOSE OF THE STUDY**

Rapid scan speeds permit 3D SD-OCT scans, which produce 3D cube data sets allowing arbitrary postprocessing of data, and in the future will benefit from image alignment and registration techniques for individual scans and from scan to scan. Using 3D SD-OCT, it is possible to gather a large amount of information about a tissue region of interest with minimal sampling error introduced by interpolation between A-scans. Tools are currently being generated to automatically align, register, and select the data needed for a specific region of interest; however, these software devices do not yet exist. One area that holds much promise for this method is the

selection of data along a 3.4-mm-diameter circle around the optic nerve head from the 3D data to more accurately measure RNFL thickness. By automatically selecting the location of the circle and measuring in exactly the same tissue location from session to session, there should be much less variation in circle placement than with current clinical TD-OCT devices. While both SD-OCT and TD-OCT can have artifact from eye movement during data acquisition, TD-OCT does not offer the possibility to align and register the data post hoc. Although this concept is still “vapor ware” for SD-OCT at the time of this writing, it is indeed feasible and has been implemented with many imaging technologies, medical and otherwise. Such alignment and registration could provide improvements in measurement reproducibility, sensitivity and specificity of disease, and progression detection. 3D data sets could also advance assessment of macular parameters such as total retinal thickness and the thicknesses of each retinal layer, including macular RNFL thickness measurements, because of higher axial resolution and scan density than possible with the currently available TD-OCT.

The purpose of this study is to determine the reproducibility and glaucoma discriminating abilities of 3D SD-OCT and TD-OCT in order to test the hypothesis that 3D SD-OCT would be superior to TD-OCT in the tested properties.

## METHODS

This study was approved by the Institutional Review Boards/Ethics Committee of the University of Pittsburgh, and adhered to the Declaration of Helsinki and Health Insurance Portability and Accountability Act regulations, with informed consent obtained from all subjects.

The study participants underwent a full ocular examination, including IOP measurements and gonioscopy, central corneal pachymetry, anterior and posterior segment biomicroscopy before and after pupil dilation, visual field testing, fundus photography, and ocular imaging with two SD-OCT devices and one TD-OCT device, all within a 6-month time period. Pharmacologic dilation was provided prior to fundus photography and OCT imaging, with tropicamide 1% and phenylephrine 2.5%. Exclusion criteria for the study were history of ocular trauma or surgery other than uncomplicated cataract surgery, best-corrected visual acuity worse than 20/40, refractive error greater than +3.0 D or less than -7.0 D, inability to view the optic nerve head or obtain acceptable imaging scans due to media opacity or poorly dilating pupil, inability to maintain fixation without movement for the duration of the 3D scan, and ocular disease or other diseases that might cause visual field abnormalities, other than glaucoma.

### VISUAL FIELD DIAGNOSIS CRITERIA

Classification as a glaucomatous or healthy subject was based on visual field results, without structural information. Humphrey 24-2 Swedish Interactive Thresholding Algorithm (Carl Zeiss Meditec, Inc, Dublin, California) visual field testing was used. The diagnosis was glaucoma if visual field mean deviation or pattern standard deviation was below 5% cutoffs, or glaucoma hemifield test was outside normal limits reproducibly in at least 2 reliable visual field tests. Visual fields were considered reliable if fixation losses, false negatives, and false positives were less than 30%, and if defects were present in a consistent location between tests. Subjects were declared healthy if visual field mean deviation, pattern standard deviation, and glaucoma hemifield test were all within normal limits for at least 2 reliable visual field tests. If glaucoma hemifield test was borderline, mean and pattern standard deviation were <10% but > 5%, or defects were inconsistent between visual fields, the subject was categorized as “glaucoma suspect” and was removed from the data set.

### OCT IMAGING

Three OCT devices were used for this study: Stratus OCT (TD-OCT), Cirrus HD-OCT (SD-OCT) (both devices from Carl Zeiss Meditec, Inc, Dublin, California), and RTVue OCT (SD-OCT) (Optovue, Inc, Fremont, California). Stratus OCT has a scanning speed of 400 A-scans per second and an axial resolution of ~8 to 10  $\mu\text{m}$ . The 2 TD-OCT scan patterns used in this study are the fast RNFL and fast macular scan. The fast RNFL pattern consists of 3 3.4-mm-diameter circles with 256 A-scans in each circle. A segmentation algorithm from our own software is applied to determine the RNFL thickness for each of the 3 scans, and then the 3 RNFL thickness profiles are averaged to determine the final profile for the scan. The fast macular scan pattern consists of 6 radial slices centered on the macula, each 6 mm long and consisting of 128 A-scans. Included scans are required to have a quality score, as output by the manufacturer’s software, of at least 6, and are judged subjectively to be free of movement artifacts or areas of signal loss within each B-scan.

The Cirrus HD-OCT and RTVue OCT data sets used were both 3D cubes, one centered on the optic nerve head and the other on the macula. Cirrus creates an array of 200×200 A-scans with an axial resolution of ~5 to 7  $\mu\text{m}$  in 1.54 seconds, covering an area of 6×6 mm. RTVue’s 3D data set is 512×101 A-scans, with an axial resolution of ~5-7  $\mu\text{m}$ , acquired in 2 seconds, covering a 4×4-mm area. Cirrus is used to determine the reproducibility of RNFL thickness measurements sampling a 3.4-mm circle centered on the optic nerve head from the optic nerve–centered 3D cube data set and macular thickness parameters from the macular 3D cube data set. For this portion of the study, we used a cohort of repeated examinations within the same visit for healthy subjects who already existed within our institutional data set. RTVue, the SD-OCT that we have had in clinical and clinical study use for more than 1 year, is used to test glaucoma discrimination ability.

3D data sets were judged for adequate image quality prior to image resampling and segmentation analysis. For Cirrus, quality score had to be greater than 7 out of 10, and for RTVue, signal strength index had to be at least 35. To judge eye movement in the optic nerve head scans, breaks in the vessels as observed in the OCT fundus image were judged to denote movement between B-scans. For the images to qualify, they had to have no movements within the 3.4-mm circle created by our software. This was accomplished in 2 ways. (1) If there were no movements in the original scan, the images could be simply processed for circular scan creation. (2) If the

image appeared to contain only small movements (no more than a vessel diameter), we used motion correction software of our own design to align the images. If the software appeared to correctly align the image without distortion on viewing the OCT fundus image, the scan was judged acceptable and was included. A description of the software methods used can be found in the "Software" section, which follows.

Once the image was aligned, software of our own design was used to locate the center of the disc and create the 3.4-mm circle. An experienced operator traced the disc margin as viewed from the OCT fundus image. The center of the disc was then automatically determined based on the disc margin, and a 3.4-mm circle was created with the disc center point at its center. If this circle went beyond the boundaries of the scan area owing to decentration of the scan on the optic nerve, this scan was eliminated from the data set. This occurred more frequently for the RTVue scans because of the smaller area covered.

For the reproducibility portion of the study, 3 macular cube scans and 3 optic nerve head scans were acquired on the Cirrus SD-OCT during the same visit. The order of scan type was varied according to the flip of a coin, with some subjects receiving the macular scans first and some receiving the optic nerve head scans first. In between each scan, subjects were asked to sit back, and then sit forward again for the next scan, to allow for realignment by the operator.

The data set for the reproducibility study consists of 3 fast macular and fast RNFL TD-OCT scans acquired on the same day for each eye in that portion of the study, and 3 macular and RNFL Cirrus 3D cube scans acquired on the same day for each eye. Both eyes could be included for an individual for the reproducibility study. The data set for the discrimination study consists of one macular and one optic nerve head RTVue 3D cube scan and one fast macular and fast RNFL TD-OCT scan set for each eye included in the study. One eye was included from each subject for the glaucoma discrimination study.

## **SOFTWARE**

Members of our Glaucoma Imaging Group developed all software used to process the raw data files for segmentation, 3D data set circular B-scan selection, and 3D OCT image alignment for OCT data analysis. Segmentation and circle selection algorithms have been previously described.<sup>11,65,66</sup> Image alignment software is currently being validated prior to publication. We used our own software for image processing and analysis rather than commercially available software to evaluate the latest, most advanced methods of analyzing SD-OCT data, and also so that we could apply similar segmentation algorithm principles to the SD-OCT and TD-OCT data sets. Commercially available software has exhibited tendencies to oversmooth the contours during segmentation and has exhibited problems with alignment of 3D data sets. At the time of the study, there was no commercial software to select circular data from 3D data sets. Most recently, one of the devices used (Cirrus) had a new software release with greater image segmentation and processing capabilities than the original software, but this has not been tested.

Segmentation algorithms for RNFL and macula were developed separately for both TD-OCT and SD-OCT data and do not apply standard thresholding techniques, which can miss peaks in signal indicative of specific layers.<sup>65</sup> TD-OCT fast RNFL raw data files are submitted to an algorithm that first determines the inner limiting membrane (ILM), defined as the first highly reflective rise. The ILM is followed by the highly reflective RNFL. The algorithm then seeks the anteriormost edge of the RPE as the second highly reflective rise and aligns all A-scans in the B-scan along the plane of the RPE. The algorithm then seeks the inner and outer borders of the RNFL along each A-scan, defining the RNFL as a wide, highly reflective peak between the ILM and RPE, which may be made up of multiple peaks, depending on noise.

Macular segmentation is slightly more complicated than peripapillary RNFL because of the numerous layers to be segmented besides the RPE.<sup>66</sup> Macular TD-OCT and SD-OCT scans are preprocessed by aligning the A-scans with cross-correlation, equalizing the pixel intensity histogram along each A-scan, and applying a modified mean filter to remove speckle noise. For segmentation, the ILM is first identified as the first highly reflective increase on the inner side. The RPE is found by identifying the 2 major peaks of each sampling line. The inner border of the second peak is the interface of the inner segment and outer segments of the photoreceptors. A gap close to this is detected as the inner border of the RPE/choroid. The distance between the ILM and inner border of the RPE/choroid is defined as the whole retinal thickness. The broadest area of lowest signal is defined as the outer retinal complex, consisting of the outer nuclear layer and inner and outer segments of the photoreceptors, layers not typically affected by glaucoma. The innermost prominent peak between the ILM and inner edge of the outer retinal complex is the macular RNFL layer. The outermost peak inside of the outer retinal complex is the outer plexiform layer. The remaining area from the outer border of the macular RNFL to the inner border of the outer plexiform layer is considered the inner retinal complex, consisting of the ganglion cells, inner plexiform layer, and inner nuclear layer. The individual layers of the retinal scans can be seen labeled in Figure 3. Software measuring total retinal, RNFL, inner retinal complex, outer retinal complex, and outer plexiform layer thicknesses has been validated for TD-OCT<sup>66</sup>; however, segmentation of layers in 3D SD-OCT data besides total retinal thickness and RNFL thickness is not as stable yet and therefore is not included for comparison.

Macular layer thickness values are calculated globally, as well as sectorally, in the sectors indicated in Figure 4. Global measurements are taken inside the outermost circle, not across the whole square of the scan. For TD-OCT and SD-OCT measurements, the outer circle has a diameter of 6 mm, the middle circle has a diameter of 3 mm, and the innermost circle has a diameter of 1 mm. For RTVue, the outer circle has a diameter of 4 mm, the middle circle has a diameter of 2 mm, and the innermost circle has a diameter of 2/3 mm, so all measurements are in proportion to the TD-OCT and SD-OCT scans, scaled down to the 4×4-mm RTVue scan.

Segmentation algorithms are developed for the 3D RNFL data set, in conjunction with the 3.4-mm circle section software. The disc margin of the scan is selected on the basis of the fundus image using spline-interpolated points placed on the outer edge of the

disc. When peripapillary atrophy makes borders difficult to distinguish based on the fundus image alone, viewing of the B-scans makes it possible to align the disc margin with the ends of Bruch's membrane. From the disc shape, the geometric center is found and the A-scans forming a 3.4-mm-diameter circle with that center are selected to form a RNFL circular B-scan, similar to that acquired by the TD-OCT. Segmentation algorithm methods described above for TD-OCT are then used for the RNFL data. Values for RNFL thickness at each A-scan are averaged to find the overall average thickness and the average thicknesses for each of the quadrants (temporal, inferior, nasal, and superior) and each of the clock hours.

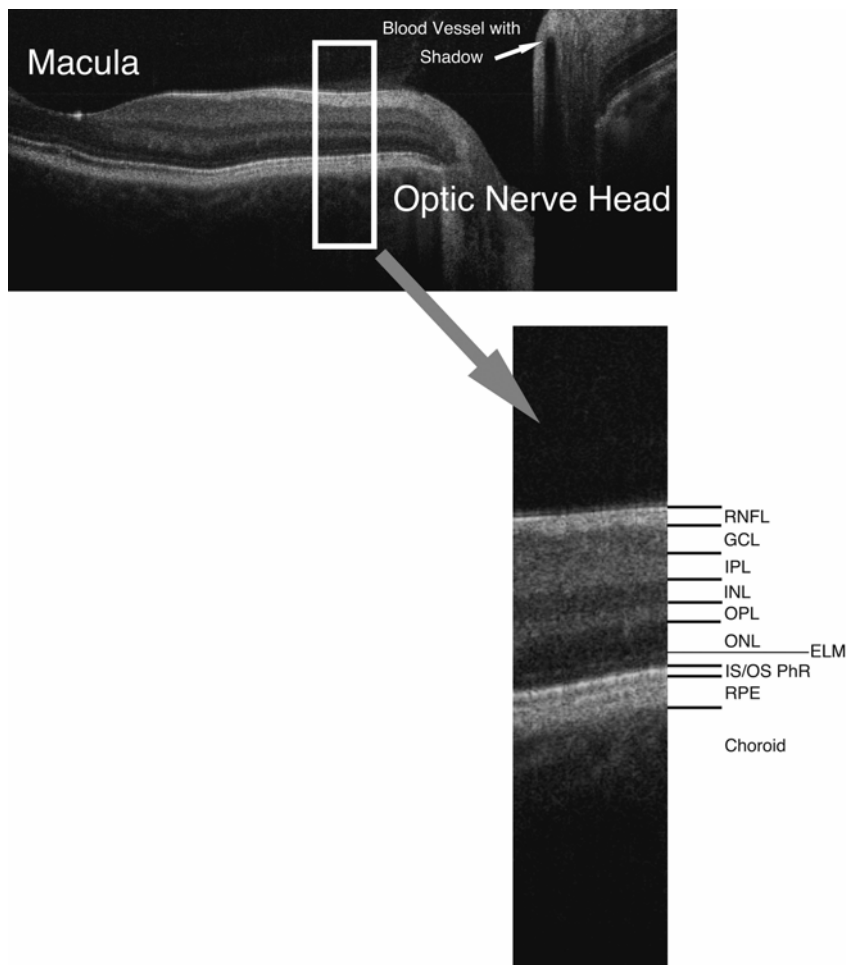


**FIGURE 3**

Spectral domain optical coherence tomography B-scan from macula to optic disc, with retinal layers labeled: RNFL, retinal nerve fiber layer; GCL, ganglion cell layer; IPL, inner plexiform layer; INL, inner nuclear layer; OPL, outer plexiform layer; ONL, outer nuclear layer; ELM, external limiting membrane; IS/OS PhR, boundary between inner and outer segments of the photoreceptors; RPE, retinal pigment epithelium.

For those 3D data sets that required alignment of B-scans in the X-direction (horizontally) due to eye motion or saccades during and between B-scan acquisition, software developed within our group is used. The software applies cross-correlation to a scaled-down version of the image to better align consecutive B-scans. This cross-correlation is applied in both the X-direction and the Z-direction (down through the A-scans) to minimize the effects of both eye saccades and movement of the eye toward or away from the device, primarily due to head motion. A 50% scaled-down version is used in order to reduce computation time for determining the shifts, which are then applied to the full version. This level of scaling down has been tested within our group to be a sufficient balance between decreasing computation time and producing accurate movement artifact reduction. Cross-correlation is done using ImageJ (National Institutes of Health, <http://rsb.info.nih.gov/ij/>) with the plug-in StackReg (Philippe Thévenaz, Biomedical Imaging Group, Swiss Federal Institute of Technology Lausanne, <http://bigwww.epfl.ch/thevenaz/stackreg/>).

### STATISTICAL ANALYSIS

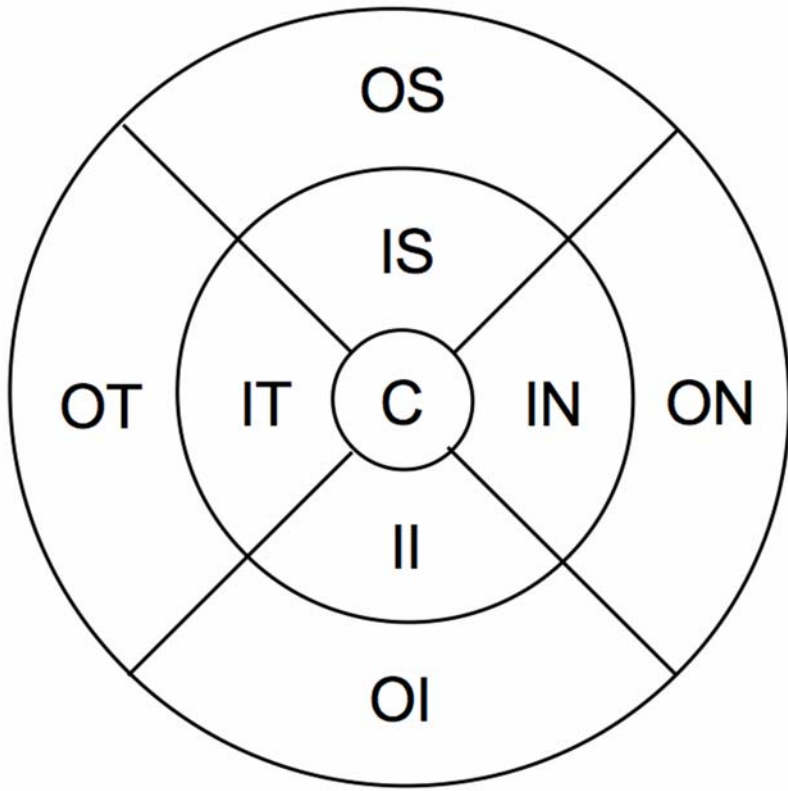
To determine the reproducibility of each scan type's segmentation software-generated parameters, linear mixed effects models are used to compute the variance components for RNFL and macular parameters. A variance function is used to represent different variance components for TD-OCT and SD-OCT. Fixed effects to describe the difference between TD-OCT and SD-OCT values are also calculated.

To test glaucoma discrimination abilities, the area under the receiver operating characteristic curves (AUCs) are calculated for each RNFL or macular parameter to evaluate sensitivity and specificity for visual field-based glaucoma diagnoses. Confidence intervals for the differences in AUC are computed using the jackknife procedure, because these are paired samples, and are used to

compare AUCs between TD-OCT parameters and SD-OCT parameters. Receiver operating characteristic (ROC) graphs are also created.

**FIGURE 4**

Areas of macular thickness segmentation: C, center; OS, outer superior; ON, outer nasal; OI, outer inferior; OT, outer temporal; IS, inner superior; IN, inner nasal; II, inner inferior; IT, inner temporal. Weighted mean is taken across the entire circle.



**RESULTS**

**SUBJECT CHARACTERISTICS**

Forty-one eyes of 21 subjects (SD-OCT) and 21 eyes of 21 subjects (TD-OCT) were used to test RNFL reproducibility. Forty eyes of 20 subjects (SD-OCT) and 21 eyes of 21 subjects (TD-OCT) were used to test macular parameter reproducibility. The 2 SD-OCT data sets are the same set of subjects, with one subject missing from the macular data set because macular scans were unintentionally not obtained during this subject’s visit. The 2 TD-OCT data sets were also the same set of subjects; however, the TD-OCT and SD-OCT data sets were different subjects, because there were no subjects who had received 3 sets of scans on both TD-OCT and SD-OCT. Subject gender and age information are shown in Table 1.

**TABLE 1. CHARACTERISTICS OF REPRODUCIBILITY STUDY SUBJECTS**

| VARIABLE           | MACULAR SCANS |             | RNFL SCANS  |             |
|--------------------|---------------|-------------|-------------|-------------|
|                    | SD-OCT        | TD-OCT      | SD-OCT      | TD-OCT      |
| Number of subjects | 20            | 21          | 21          | 21          |
| Number of eyes     | 40            | 21          | 41          | 21          |
| Male : female      | 6:14          | 9:12        | 7:14        | 9:12        |
| Age (mean ± SD)    | 44.5 ± 14.3   | 48.6 ± 14.1 | 44.0 ± 14.1 | 48.6 ± 14.1 |

RNFL, retinal nerve fiber layer; SD, standard deviation; SD-OCT, Cirrus OCT; TD-OCT, Stratus OCT.

For both TD-OCT and SD-OCT, 83 eyes of 83 subjects were used to evaluate RNFL and 74 eyes of 74 subjects to evaluate macular glaucoma discrimination. Nine of 83 eyes (11%) from the RNFL data set were excluded from the macular data set because of inadequate quality or no macular scan obtained during their visit. Poor quality of the macular scan set was defined as low OCT signal,

too much eye movement during the scan (as described above), or excessive failure in the 3D data set macular segmentation as judged subjectively. Subject genders, ages, and visual field information are shown in Table 2. Average visual field mean deviation of  $-3.70 \pm 4.22$  in glaucoma subgroup is indicative of early to moderate glaucomatous damage.

**TABLE 2. CHARACTERISTICS OF DISCRIMINATION STUDY SUBJECTS**

| VARIABLE               | MACULAR SCANS   |                  | RNFL SCANS      |                  |
|------------------------|-----------------|------------------|-----------------|------------------|
|                        | HEALTHY         | GLAUCOMA         | HEALTHY         | GLAUCOMA         |
| Number of subjects     | 47              | 27               | 53              | 30               |
| Male : female          | 12:36           | 5:21             | 13:40           | 6:24             |
| Age (mean $\pm$ SD)    | 53.0 $\pm$ 9.3  | 58.5 $\pm$ 11.1  | 52.2 $\pm$ 9.4  | 59.4 $\pm$ 10.9  |
| VF MD (mean $\pm$ SD)  | 0.25 $\pm$ 1.15 | -3.70 $\pm$ 4.41 | 0.16 $\pm$ 1.23 | -3.70 $\pm$ 4.22 |
| VF PSD (mean $\pm$ SD) | 1.49 $\pm$ 0.28 | 4.67 $\pm$ 3.75  | 1.51 $\pm$ 0.28 | 4.63 $\pm$ 3.85  |

RNFL, retinal nerve fiber layer; SD, standard deviation; VF MD, visual field mean deviation; VF PSD, visual field pattern standard deviation.

## REPRODUCIBILITY

For RNFL, SD-OCT and TD-OCT variances and the variance function, which is equal to TD-OCT variance over SD-OCT variance, and its confidence interval can be found in Table 3. All variance components mentioned are in square root terms. The fixed effects models for each parameter all had confidence intervals for the difference between SD-OCT and TD-OCT that included zero, except for clock hours 8 and 12; therefore, there is no relative bias between the 2 devices in all measurements except these two. Clock hour 12 had a confidence interval of 1.39 to 26.97, indicating that in this sector, TD-OCT measurements tended to be thicker than SD-OCT measurements. In clock hour 8, the confidence interval was 5.54 to 26.16, also indicating that in this sector TD-OCT measurements tended to be thicker than SD-OCT measurements.

For macular parameters, SD-OCT and TD-OCT variances and the variance function, which is equal to TD-OCT variance over SD-OCT variance, and its confidence interval can be found in Table 4. All variance components are in square root terms. The results for macular reproducibility were not as straightforward as for RNFL, with weighted mean total retinal thickness and 2 of the 4 inner sector total retinal thickness parameters including one in their confidence intervals, and inner temporal total retinal thickness being the only parameter tested out of both scanning areas to have one above its confidence interval. All fixed effects models included zero, except outer superior retinal thickness, which had a confidence interval of  $-27.91$  to  $-7.15$ ; inner superior retinal thickness, which had a confidence interval of  $-32.65$  to  $-9.25$ ; and the center, which had a confidence interval of 5.31 to 31.76, indicating that SD-OCT measurements were thicker superiorly than TD-OCT measurements, and central TD-OCT measurements were thicker than SD-OCT measurements.

Narrow confidence intervals for the difference between TD-OCT and SD-OCT were found in this study, indicating that the number of patients was sufficient to make generalizable observations about the difference between the 2 devices' reproducibility.

## GLAUCOMA DISCRIMINATION

AUC results for RNFL parameters, and the *P* value and upper and lower bounds of the confidence interval of the difference between TD-OCT and SD-OCT, can be seen in Table 5. With alpha level set prior to data acquisition at 0.05, there was no significant difference in glaucoma discrimination between SD-OCT and TD-OCT for any global, quadrant, or clock hour RNFL thickness measurement.

AUC results for macular parameters, and the *P* value and upper and lower bounds of the confidence interval of the difference between TD-OCT and SD-OCT, can be seen in Table 6. There was no significant difference in glaucoma discrimination between SD-OCT and TD-OCT for any global or sectoral total macular retinal thickness measurement. Comparison was made of the discrimination ability of TD-OCT mean macular retinal thickness averaged both as a simple mean and as a weighted mean, taking into account the distance from the center of the macula. As may be expected, the weighted mean provided better discrimination; however, the difference between the two was not statistically significant (*P* = .096). There was a small but statistically significant difference between weighted mean macular RNFL thickness discrimination of TD-OCT and SD-OCT, though the difference between TD-OCT weighted mean macular RNFL and the unweighted mean macular RNFL from SD-OCT was not statistically significant.

Narrow confidence intervals for the difference between TD-OCT and SD-OCT were found in this study, indicating that the number of patients was sufficient to make generalizable observations about the difference between the two devices' discrimination.

## CASE STUDIES

In addition to the statistically tested research, it is important to understand the appearance and utility of SD-OCT in healthy and glaucomatous eyes. While the objective quantitative data are essential, qualitative assessment of the scans and thickness maps provides important information as well.

**TABLE 3. PERIPAPILLARY RETINAL NERVE FIBER LAYER THICKNESS REPRODUCIBILITY RESULTS**

| PARAMETER* | SD-OCT†<br>VARIANCE | TD-OCT‡<br>VARIANCE | VARIANCE<br>FUNCTION LB | VARIANCE<br>FUNCTION§ | VARIANCE<br>FUNCTION UB |
|------------|---------------------|---------------------|-------------------------|-----------------------|-------------------------|
| Global     | 8.20                | 7.38                | 0.69                    | 0.90                  | 1.17                    |
| Temporal   | 13.51               | 23.97               | 1.36                    | 1.77                  | 2.32                    |
| Superior   | 14.97               | 28.36               | 1.45                    | 1.90                  | 2.47                    |
| Nasal      | 33.75               | 42.22               | 0.96                    | 1.25                  | 1.63                    |
| Inferior   | 12.56               | 24.62               | 1.50                    | 1.96                  | 2.56                    |
| CH 12      | 34.43               | 63.32               | 1.41                    | 1.84                  | 2.39                    |
| CH 1       | 25.71               | 65.05               | 1.93                    | 2.53                  | 3.31                    |
| CH 2       | 47.68               | 73.42               | 1.18                    | 1.54                  | 2.00                    |
| CH 3       | 45.47               | 64.89               | 1.10                    | 1.43                  | 1.85                    |
| CH 4       | 36.12               | 50.53               | 1.07                    | 1.40                  | 1.82                    |
| CH 5       | 21.25               | 38.27               | 1.38                    | 1.80                  | 2.35                    |
| CH 6       | 34.35               | 74.44               | 1.66                    | 2.17                  | 2.83                    |
| CH 7       | 28.40               | 43.77               | 1.18                    | 1.54                  | 2.01                    |
| CH 8       | 18.05               | 40.61               | 1.72                    | 2.25                  | 2.94                    |
| CH 9       | 21.02               | 32.85               | 1.19                    | 1.56                  | 2.05                    |
| CH 10      | 16.60               | 31.79               | 1.47                    | 1.92                  | 2.49                    |
| CH 11      | 28.90               | 53.86               | 1.43                    | 1.86                  | 2.43                    |

CH, clock hour; LB, lower bound (of variance function confidence interval); SD-OCT, spectral domain ocular coherence tomography; TD-OCT, time domain ocular coherence tomography; UB, upper bound (of variance function confidence interval).

\*All parameters are retinal nerve fiber layer thickness measurements in the named sectors. Variance components are in square root terms.

†Cirrus OCT.

‡Stratus OCT.

§TD-OCT variance/SD-OCT variance.

### Healthy Eye

Understanding of the structures that can be visualized on OCT in a healthy eye is necessary before scans of glaucomatous or other diseased eyes can be interpreted. This case study of a healthy subject is presented using a variety of SD-OCT devices and TD-OCT for comparison. The subject is a 23-year-old woman with an IOP of 16 mm Hg, reproducibly full visual fields, and healthy-appearing optic nerves (Figure 5). TD-OCT scans appear normal for the subject's age. The subject's right eye is presented here.

Figure 3 is a linear scan through the macula extending to the optic nerve head. In the macula, 10 distinct layers are present: plexiform layers, RFNL, photoreceptor inner segment–outer segment junction, RPE and choriocapillaris highly scattering, resulting in bright reflections, and RGC and nuclear layers (cell bodies) weakly backscattering, resulting in darker areas. A sharp increase in backscattering is present at the vitreoretinal interface across the image. The foveal depression can be seen clearly at the left edge of the B-scan, where the inner retinal layers are absent and photoreceptor layers are thicker. The innermost layer, which is highly scattering and therefore appears white on a black/white scale, or red on a color scale, which thins to nothing at the macula, is the RNFL. It is thicker nasal to the fovea and is one of the most easily segmented intraretinal layers, owing to its high reflectivity. The weakly reflective layers below the RNFL are the ganglion cell layer, inner plexiform layer, inner nuclear layer, outer plexiform layer, and outer nuclear layer. The ganglion cell layer is thickest parafoveally, where there are the most ganglion cell bodies. The moderately scattering layer between the ganglion cell layer and inner nuclear layer is the inner plexiform layer, and the outer plexiform layer is the moderately reflective layer above the outer nuclear layer, the least reflective layer in this image. The external limiting membrane (ELM) can be seen as a thin, somewhat highly backscattering layer in the posterior aspect of the outer nuclear layer. The even more highly backscattering thin layer posterior to ELM, just anterior to the RPE, is understood to be the boundary between the photoreceptor inner and outer segments, with its high reflectivity caused by tight alignment of the cilium connecting the inner and outer segments. The RPE is visualized as the wider bright band posterior to the photoreceptors and is not always distinguishable from the also brightly reflective choriocapillaris, which is highly reflective due to the amount of blood in that layer. Beyond this is the larger vasculature of the choroid, which may be more or less visible depending on the wavelength of light used and the penetration it allows. Blood vessels throughout the tissue layers may often be identified by the shadow they cast throughout the sample, as the blood

contained in them is highly reflective at OCT light source wavelengths.

**TABLE 4. MACULAR THICKNESS REPRODUCIBILITY RESULTS**

| <b>PARAMETER*</b> | <b>SD-OCT†<br/>VARIANCE</b> | <b>TD-OCT‡<br/>VARIANCE</b> | <b>VARIANCE<br/>FUNCTION LB</b> | <b>VARIANCE<br/>FUNCTION§</b> | <b>VARIANCE<br/>FUNCTION UB</b> |
|-------------------|-----------------------------|-----------------------------|---------------------------------|-------------------------------|---------------------------------|
| Weighted mean     | 1.77                        | 2.11                        | 0.91                            | 1.19                          | 1.55                            |
| Outer temporal    | 2.94                        | 4.22                        | 1.10                            | 1.44                          | 1.87                            |
| Outer superior    | 2.33                        | 5.68                        | 1.87                            | 2.44                          | 3.18                            |
| Outer nasal       | 3.00                        | 5.21                        | 1.33                            | 1.74                          | 2.27                            |
| Outer inferior    | 3.76                        | 5.28                        | 1.08                            | 1.40                          | 1.83                            |
| Inner temporal    | 8.51                        | 6.20                        | 0.56                            | 0.73                          | 0.95                            |
| Inner superior    | 4.65                        | 5.76                        | 0.95                            | 1.24                          | 1.62                            |
| Inner nasal       | 7.26                        | 8.93                        | 0.94                            | 1.23                          | 1.61                            |
| Inner inferior    | 3.80                        | 5.84                        | 1.18                            | 1.54                          | 1.01                            |
| Center            | 36.53                       | 32.84                       | 0.69                            | 0.90                          | 1.17                            |
| Weighted RNFL     | 1.54                        | 2.34                        | 1.16                            | 1.52                          | 1.98                            |

LB, lower bound (of variance function confidence interval); RNFL, retinal nerve fiber layer; SD-OCT, spectral domain ocular coherence tomography; TD-OCT, time domain ocular coherence tomography; UB, upper bound (of variance function confidence interval).

\*Weighted mean and sectoral parameters are total retinal thickness measurements. Weighted RNFL is the weighted mean RNFL thickness measurement. Weighted means are calculated across the entire circle shown in Figure 4. Variance components are in square root terms.

†Cirrus OCT.

‡Stratus OCT.

§TD-OCT variance/SD-OCT variance.

Figure 6 presents a variety of macular SD-OCT scan types that are currently available. Scan A is the RTVue MM5 scan pattern, consisting of a dense 5×5-mm grid of linear scans around the macula. Individual OCT scans, as well as a thickness map, can be shown using this scan pattern. Scan B is the RTVue MM7 scan pattern (7×7-mm square), with retinal thickness displayed as a color map. It can be used primarily to visualize thickness differences between the superior and inferior hemispheres, which may be relevant in glaucoma cases. C is an ultrahigh-resolution, high transverse density (8000 A-scan) line scan obtained on an experimental SD-OCT developed at Massachusetts Institute of Technology with axial resolution of ~3.5 μm, allowing for excellent retinal layer detail. D is a similar ultrahigh-resolution high transverse density line scan from a Bioptigen research SD-OCT system (Bioptigen; Research Triangle Park, North Carolina; light source: Broadlighter, Superlum, Cork, Ireland), also exhibiting tremendous detail in the retinal layers, in a scan from the macula to the optic nerve head. E presents a 3D visualization of the macula created by a raster scan. The OCT fundus image is in the upper left with B-scan slices in the upper right and lower left from the position of the red and green lines on the OCT fundus image, respectively, and a 3D rendering in the lower right. The OCT fundus image is generated by summing the reflectance through the whole of each A-scan to establish the reflectance for each corresponding A-scan point represented by each pixel of the OCT fundus image.

Scans across the optic nerve head are valuable for looking at abnormalities in the optic nerve head due to glaucoma, disc edema, or papilledema, or other diseases affecting the optic nerve head structure. In the healthy eye, OCT scans can typically visualize physiologic cupping in the disc, particularly in the case where the subject has somewhat tilted discs due to myopia, as in this case. The RNFL thickens approaching the neuroretinal rim, and where the nerve fibers bend down toward the cup, they typically are somewhat less reflective, because they are no longer perpendicular to the light beam. The termination of the RPE, choriocapillaris, and Bruch's membrane together can be clearly seen on either side of the optic nerve head, and their termination can be used as a landmark for defining the disc margin in 3D optic nerve head data sets. However, their termination can frequently be obscured by blood vessels, resulting in difficulty identifying the disc margin either manually or using intelligent algorithms for automatic landmark detection. These images can be helpful for visualizing focal changes or overall cup shape changes in an individual, but developing a normative database for optic nerve head shapes is extremely difficult, given the wide natural variation between eyes, so it is not as valuable for identifying whether someone is in the early stages of glaucoma, based on just a single examination. However, the optic nerve head scans can be examined for common signs of glaucoma such as a large cup relative to disc size and a thin neuroretinal rim.

**TABLE 5. PERIPAPILLARY RETINAL NERVE FIBER LAYER THICKNESS  
GLAUCOMA DISCRIMINATION RESULTS**

| VARIABLE* | SD-OCT† | TD-OCT AUC‡ | DIFFERENCE LB | DIFFERENCE§ | DIFFERENCE UB | P¶   |
|-----------|---------|-------------|---------------|-------------|---------------|------|
|           | AUC     |             |               |             |               |      |
| Global    | 0.746   | 0.812       | -0.007        | 0.066       | 0.138         | .077 |
| Temporal  | 0.620   | 0.635       | -0.090        | 0.015       | 0.119         | .785 |
| Nasal     | 0.676   | 0.763       | -0.023        | 0.086       | 0.195         | .120 |
| Inferior  | 0.770   | 0.805       | -0.044        | 0.035       | 0.115         | .382 |
| Superior  | 0.737   | 0.782       | -0.038        | 0.045       | 0.128         | .290 |
| CH 1      | 0.711   | 0.746       | -0.057        | 0.035       | 0.129         | .451 |
| CH 2      | 0.683   | 0.723       | -0.069        | 0.040       | 0.149         | .475 |
| CH 3      | 0.647   | 0.737       | -0.029        | 0.090       | 0.209         | .137 |
| CH 4      | 0.665   | 0.730       | -0.056        | 0.065       | 0.187         | .291 |
| CH 5      | 0.730   | 0.740       | -0.088        | 0.010       | 0.108         | .844 |
| CH 6      | 0.734   | 0.786       | -0.042        | 0.052       | 0.147         | .279 |
| CH 7      | 0.738   | 0.745       | -0.078        | 0.007       | 0.092         | .869 |
| CH 8      | 0.612   | 0.606       | -0.134        | -0.005      | 0.123         | .937 |
| CH 9      | 0.575   | 0.597       | -0.102        | 0.022       | 0.147         | .726 |
| CH 10     | 0.598   | 0.592       | -0.105        | -0.006      | 0.093         | .904 |
| CH 11     | 0.631   | 0.631       | -0.107        | 0.000       | 0.108         | .996 |
| CH 12     | 0.733   | 0.806       | -0.018        | 0.073       | 0.163         | .117 |

AUC, area under the receiver operating characteristic curve; CH, clock hour; LB, lower bound (of variance function confidence interval); UB, upper bound (of variance function confidence interval).

\*All parameters are retinal nerve fiber layer thickness measurements.

†RTVue OCT.

‡Stratus OCT.

§TD-OCT AUC minus SD-OCT AUC.

¶Significance level of difference.

Figure 7 presents a variety of optic nerve scans. A is selected slices from a 3D data set obtained by Cirrus HD-OCT, with the center vertical and horizontal B-scans displayed. B is a similar 3D data set from RTVue, with shown B-scans located in the periphery of the scan at the location of the red and green lines on the OCT fundus image. Vessel discontinuities at the top of the OCT fundus image are indicative of eye motion between horizontal B-scans. C is RTVue's NHM4 pattern, made up of a combination of radial and circular scans centered on the optic nerve head, as can be seen overlaid on the colored retinal nerve fiber thickness map. This scan pattern produces a topographic analysis of the optic nerve head cup, rim, and disc margin, as well as a map of the peripapillary RNFL. Bright red and yellow colors indicate a thick, healthy RNFL, with superior and inferior nerve bundles clearly shown. The disc margin is shown at the center of the RNFL thickness color map and is automatically divided into cup (light gray) and rim (dark gray). Both a circular and a radial B-scan are shown, as well as the fundus camera's view of the optic nerve head, and segmentation of the RNFL thickness along the 3.4-mm-diameter circle.

The type of OCT scan most commonly used by glaucoma specialists for assessment is the 3.4-mm-diameter circumpapillary scan, which is used to measure the thickness of the RNFL. By sampling this circle around the optic nerve head, an assessment of nearly all of the RGC axonal projections that constitute the RNFL can be obtained. This is very important for determining the presence and progression of glaucoma. The circular scan is presented in an "unwrapped" form and can be analyzed for RNFL thickness globally, by quadrants, by clock hours, by individual A-scan, or by other methods of dividing up the circle. Thickness typically varies across the scans, with the nerve bundles superotemporally and inferotemporally and, to a lesser extent, superonasally and inferonasally. A thickness graph illustrating the RNFL in a temporal-superior-nasal-inferior-temporal (TSNIT) pattern at a gross level shows the classic double-hump pattern. In reality, most healthy eyes have 4 humps, with 2 superiorly and 2 inferiorly, or sometimes a thickest area inferotemporally with a "shoulder" to that peak inferonasally. Examination of the OCT actually reveals not 4 "humps" but rather 4 fusiform regions of thickest RNFL corresponding to the peaks in the A-scan graph. This quadrifusiform pattern is typical of healthy eyes. Vessels are also evident from the shadowing they cause in the RNFL scans, resulting in dark columns extending vertically below vessels, most obviously seen in the normally highly reflective RPE layer.

Figure 7D presents the SD-OCT 3.4-mm circular scan centered on the optic nerve head. The RTVue SD-OCT repeats this scan 4 times and then averages to obtain final RNFL thickness values, which are displayed in the wheel-shaped grid below the scan. Shadows

caused by blood vessels are quite clear in this scan pattern as the circle of the scan cuts nearly perpendicular to them. Five shadows in the superior bundle, 4 in the inferior bundle and 1 slightly inferior of nasal are present in this subject.

**TABLE 6. MACULAR THICKNESS GLAUCOMA DISCRIMINATION RESULTS.**

| VARIABLE*       | SD-OCT† | TD-OCT‡ | DIFFERENCE LB | DIFFERENCE§ | DIFFERENCE |      |
|-----------------|---------|---------|---------------|-------------|------------|------|
|                 | AUC     | AUC     |               |             | UB         | P¶   |
| Weighted mean   | 0.741   | 0.749   | -0.061        | 0.008       | 0.077      | .823 |
| Unweighted mean | 0.741*  | 0.703   | -0.112        | -0.037      | 0.037      | .326 |
| Outer temporal  | 0.749   | 0.809   | -0.017        | 0.059       | 0.135      | .128 |
| Outer superior  | 0.727   | 0.733   | -0.085        | 0.006       | 0.097      | .899 |
| Outer nasal     | 0.676   | 0.662   | -0.102        | -0.015      | 0.073      | .745 |
| Outer inferior  | 0.795   | 0.755   | -0.116        | -0.040      | 0.036      | .298 |
| Inner temporal  | 0.680   | 0.738   | -0.058        | 0.059       | 0.175      | .323 |
| Inner superior  | 0.644   | 0.715   | -0.027        | 0.071       | 0.169      | .155 |
| Inner nasal     | 0.668   | 0.687   | -0.093        | 0.020       | 0.133      | .733 |
| Inner inferior  | 0.674   | 0.671   | -0.105        | -0.004      | 0.097      | .945 |
| Center          | 0.504   | 0.587   | -0.163        | 0.083       | 0.328      | .509 |
| Weighted RNFL   | 0.575   | 0.771   | 0.022         | 0.196       | 0.371      | .028 |
| Unweighted RNFL | 0.575*  | 0.742   | -0.011        | 0.168       | 0.346      | .065 |

AUC, area under the receiver operating characteristic curve; LB, lower bound (of variance function confidence interval); UB, upper bound (of variance function confidence interval).

\*Weighted mean and sectoral parameters are total retinal thickness measurements. Weighted RNFL is the weighted mean RNFL thickness measurement. Weighted means are calculated across the entire circle shown in Figure 4. Unweighted mean and RNFL compares unweighted mean retinal thickness and RNFL thickness TD-OCT variables with weighted SD-OCT variables, because unweighted SD-OCT variables are not available.

†RTVue OCT.

‡Stratus OCT.

§TD-OCT AUC minus SD-OCT AUC.

¶Significance level of difference.

All 3 of these types of scans (a 3.4-mm circumpapillary scan centered on the optic nerve head, 6 4-mm radial scans centered on the optic nerve head, and 6 6-mm radial scans centered on the fovea) were initially used with TD-OCT, where a single set of the macula and optic nerve head data sets are radial scans centered on the macula or optic nerve head, respectively, and the RNFL circle was acquired alone in OCT 1000 and OCT 2000, and in 3 rapid consecutive scans with Stratus OCT, with averaging of the 3 scans for better reproducibility of measures. With SD-OCT, a variety of patterns is now available, because of the improvement in acquisition speed. For the macula, much denser sampling grids can be acquired, or a variety of lines can be taken vertically to compare the superior and inferior hemispheres, similar to the glaucoma hemifield test used by Swedish interactive thresholding algorithm (SITA) and other visual field testing (Carl Zeiss Meditec, Inc, Dublin, California). On the optic nerve head, a mixture of radial and circular scans can be acquired together. Either the macula or optic nerve head, or specific retinal areas of damage, can have a 3D raster scan performed to give the most complete data regarding the retinal structure in that region. Additionally, high-density line scans in areas of interest can be acquired.

#### **Glaucomatous Eye: Early Focal Defect**

One of the areas where SD-OCT is able to provide valuable information is in the identification of early global thinning or, especially, focal defects due to the early to moderate stages of glaucoma. This case study presents a 63-year-old white woman with IOP of 14 to 17 mm Hg. Right eye visual field shows a localized superior paracentral defect (Figure 8B). The optic nerve head shows a thin inferior temporal neuroretinal rim corresponding to the visual field defect (Figure 8A), and the TD-OCT nicely demonstrates the focally thin RNFL in the same region (Figure 8C and D). This is evident in the tomogram (Figure 8C), the A-scan profile graph, and the clock hour and quadrant comparisons to the normative database (Figure 8D). The A-scan profile graph shows the very steep region of RNFL loss in this focal defect inferior temporally. This defect corresponds well with SD-OCT identification of focally thin RNFL inferior temporally, illustrated in this case using RTVue SD-OCT (Figure 9). This defect can be seen in the RNFL A-scan profile graph (4

circumpapillary scans with 3.4-mm diameter centered on the optic nerve, Figure 9A) and NHM4 (optic nerve head radial and circular scan combination, Figure 9C) scan patterns, as well as in the 3D cube data set (Figures 9B and D). The RTVue RNFL scan in Figure 9A shows a notch inferior temporally, similar to that seen on the Stratus TD-OCT in Figure 8D, and the NHM4 scan in Figure 9C clearly shows the RNFL tissue loss with the area mapped dark blue and black. The RNFL loss can be seen in the 3D cube data set in Figure 9B in the B-scan at the location of the green line on the en face image, on the left side of the B-scan. The macular scan in Figure 9D shows a region of thin retina corresponding spatially with the area of visual field loss.

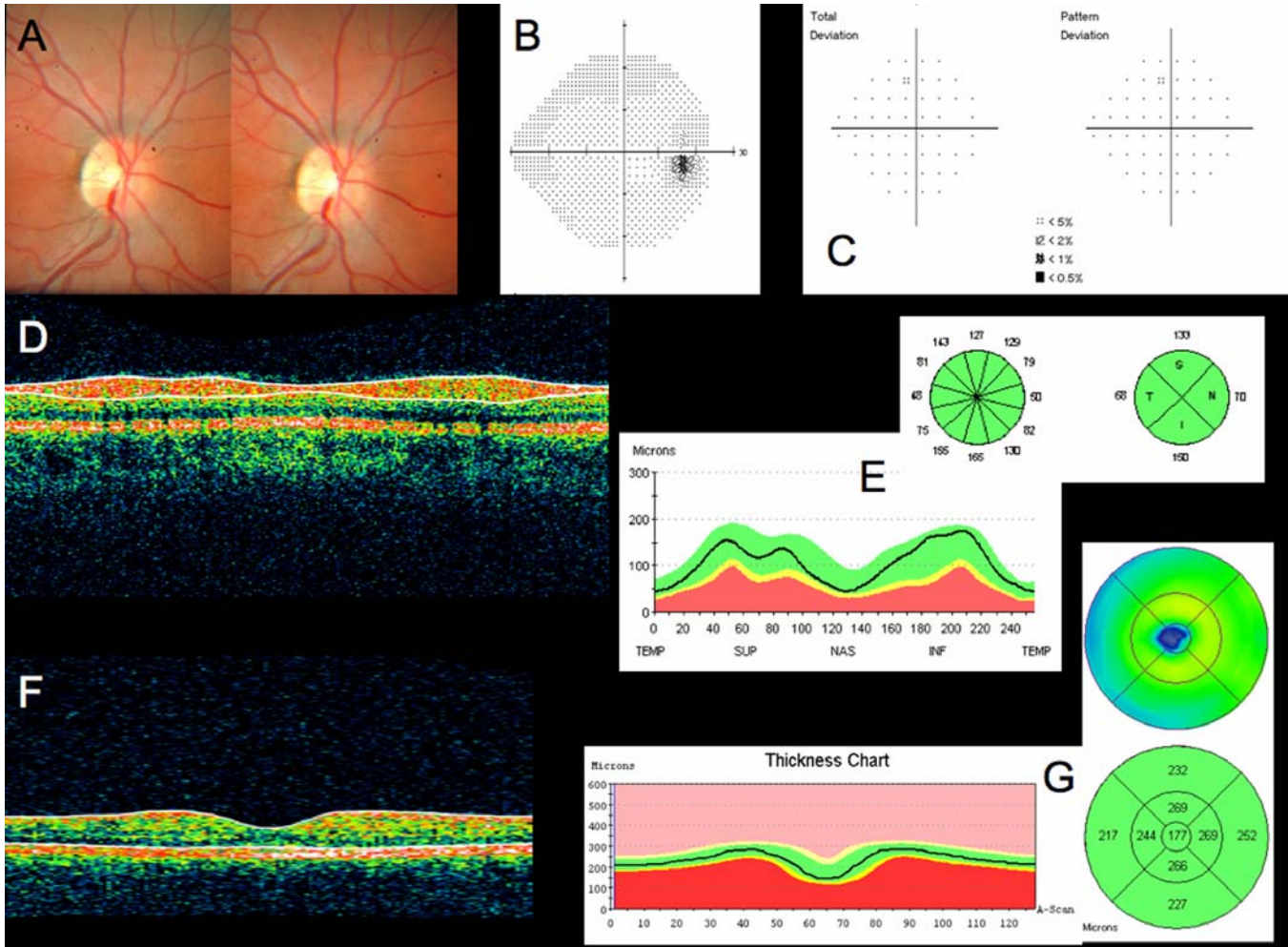


**FIGURE 5**

Conventional testing images from healthy case study: A, Stereoscopic disc photographs of a 23-year-old white woman's healthy right eye. B, Humphrey SITA 24-2 threshold map of healthy right eye. C, Total deviation and pattern deviation maps showing no significant deviation from normative values. D, Time domain ocular coherence tomography (TD-OCT) retinal nerve fiber layer (RNFL) thickness OCT scan, with white lines delineating RNFL boundaries. The white lines are automatically placed by software that automatically identifies the tissue borders of interest, but should always be checked by the clinician for accuracy. E, RNFL segmentation results superimposed on normative database. Green is within normal limits (5th to 95th percentile), yellow is borderline (1st to 4th percentile) and red is outside normal limits (below the 1st percentile). Wheels present quadrant and clock hour averaged thicknesses. All green results indicate RNFL thickness is within normal limits. F, TD-OCT macular thickness OCT scan, with white lines designating total retinal thickness segmentation results. G, Single macular scan and macular map results. Single scan and overall measured thicknesses are compared to normative values. Map represents thicker measurements with warmer colors, and thinner measurements with cooler colors (eg, the fovea is dark blue, as the thinnest region in the healthy eye).

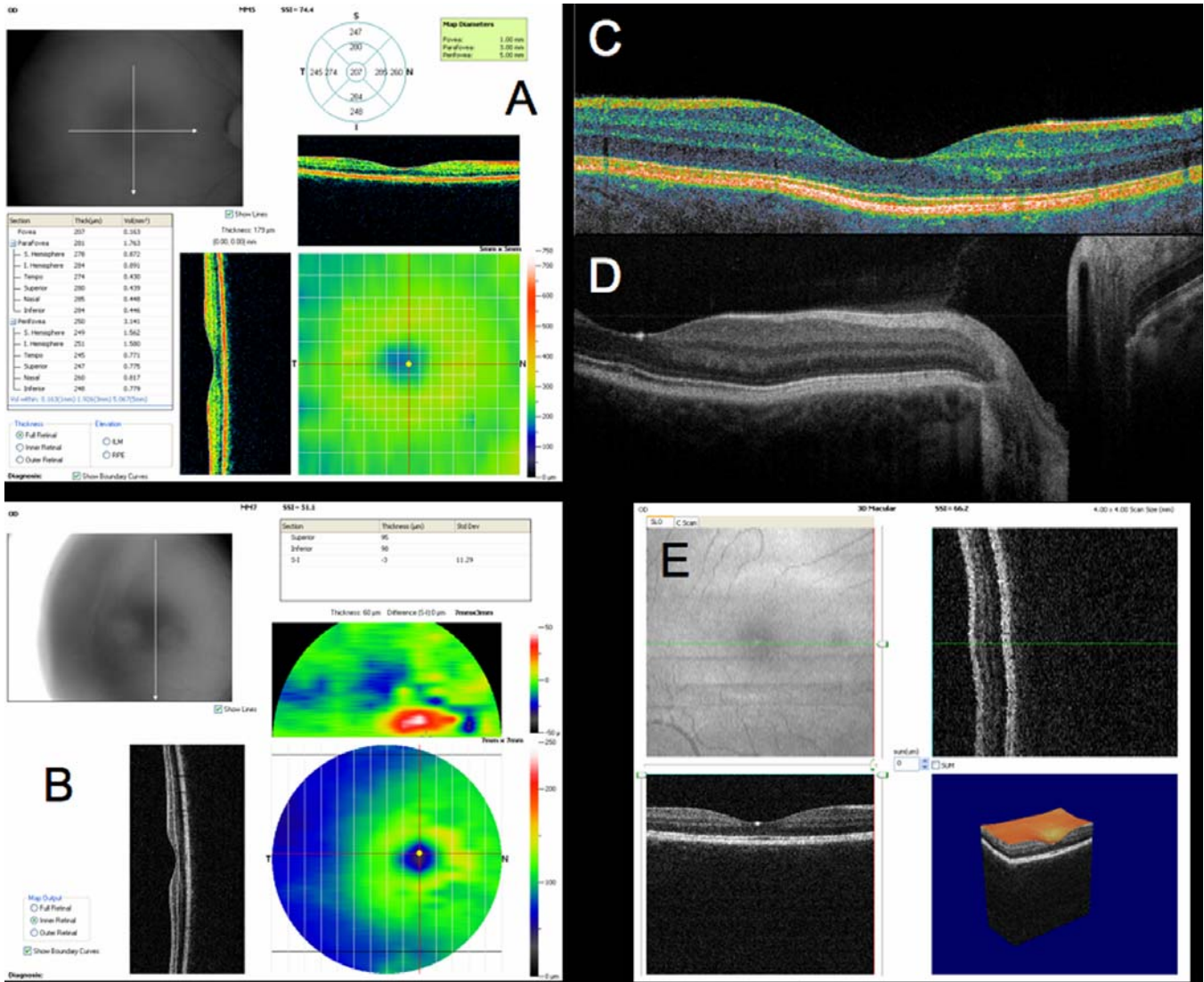


**FIGURE 6**

Macular spectral domain optical coherence tomography (SD-OCT) images from healthy case study shown in Figure 5. A, RTVue MM5 output, with fundus camera view, vertical and horizontal OCT scans through macula, macular map, and tabular thickness measurements. B, RTVue MM7 output, with macular map, map of superior-inferior thickness differences, and vertical OCT B-scan through the macula. The red area indicating a large difference between the superior and inferior hemispheres at that point is an artifact of slight decentration of the macula vertically in that scan. C, High-resolution color mapped SD-OCT line scan through macula acquired by research device created at Massachusetts Institute of Technology, displaying retinal layers clearly. D, High-resolution grayscale SD-OCT line scan through macula and optic nerve head acquired by Biotigen SD-OCT device. E, Macular 3D data set acquired by RTVue SD-OCT. Upper left is the OCT fundus image. Lower left and upper right B-scans are at the locations of the green and red lines on the OCT fundus image, respectively. 3D representation is at lower right.

**Glaucomatous Eye: Advanced Global Loss**

SD-OCT can also be used to provide clinically useful information in patients who have advanced, global glaucoma injury with visual field damage corresponding to more advanced, overall RNFL loss. In this case study, the subject is a 71-year-old woman with moderate to advanced visual field loss in her left eye (mean deviation -9.58, pattern standard deviation 10.79, Figure 10B). Stereoscopic disc photography reveals moderate to marked cupping due to overall loss of neuroretinal rim tissue, as well as notching

at 1 o'clock and 5 o'clock (Figure 10A). TD-OCT RNFL scans reveal overall thinning, but the segmentation algorithm oversmooths the data, leading to a slight underestimation of thickness in the superior RNFL. RTVue circumpapillary RNFL and NHM4 scans show an overall loss of RNFL thickness, with reduced thickness of the 2 main nerve fiber bundles, particularly the inferotemporal bundle (Figure 11A and E). The NHM4 scan shows noteworthy overall loss of tissue, with a substantial part of the scan thin enough to be dark blue or black, and also presents additional localized thinning at 1 and 5 o'clock, similar to the rim tissue loss on the disc photo (Figure 11E). Optic nerve head cupping can be observed in the 3D raster scan and NHM4 scan (Figure 11B and E). Overall thinning can also be seen in the macula, particularly temporally (Figure 11C). Figure 11D displays the inner retinal thickness specifically, using a relatively new segmentation algorithm that allows segmentation of the intraretinal layers beyond simply total retinal thickness and macular RNFL thickness. This algorithm also permits superior to inferior macular comparison by subtraction, as shown in the upper panel of Figure 11D. This demonstrates asymmetry in inner retinal thickness, with the inner retina thinner inferiorly than superiorly, consistent with the RNFL thickness shown in Figures 10 C and D and 11A and the visual field shown in Figure 10B. Note on the visual field (Figure 10B) that while there is perimetric damage both above and below the horizontal meridian, with a superior nasal defect and an inferior paracentral scotoma, the inferior defect is considerably deeper than the superior one, as borne out by the TD-OCT and SD-OCT.

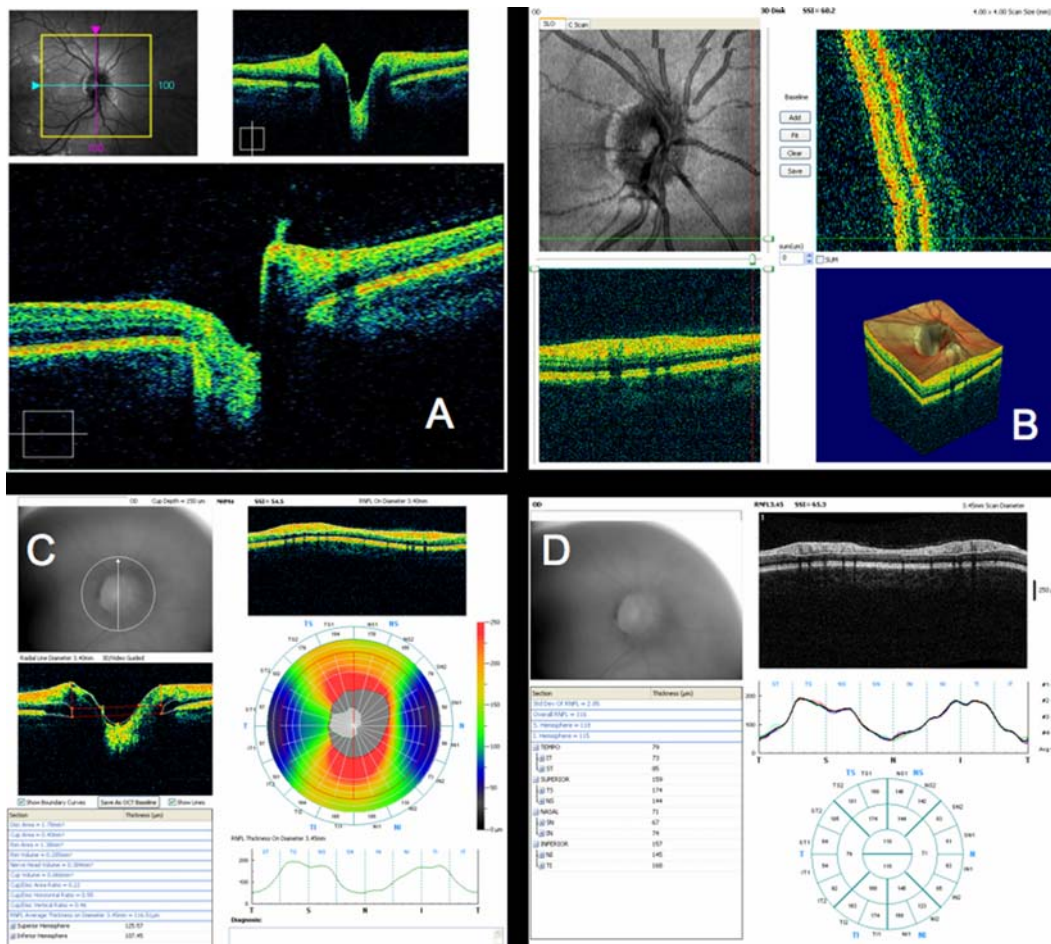
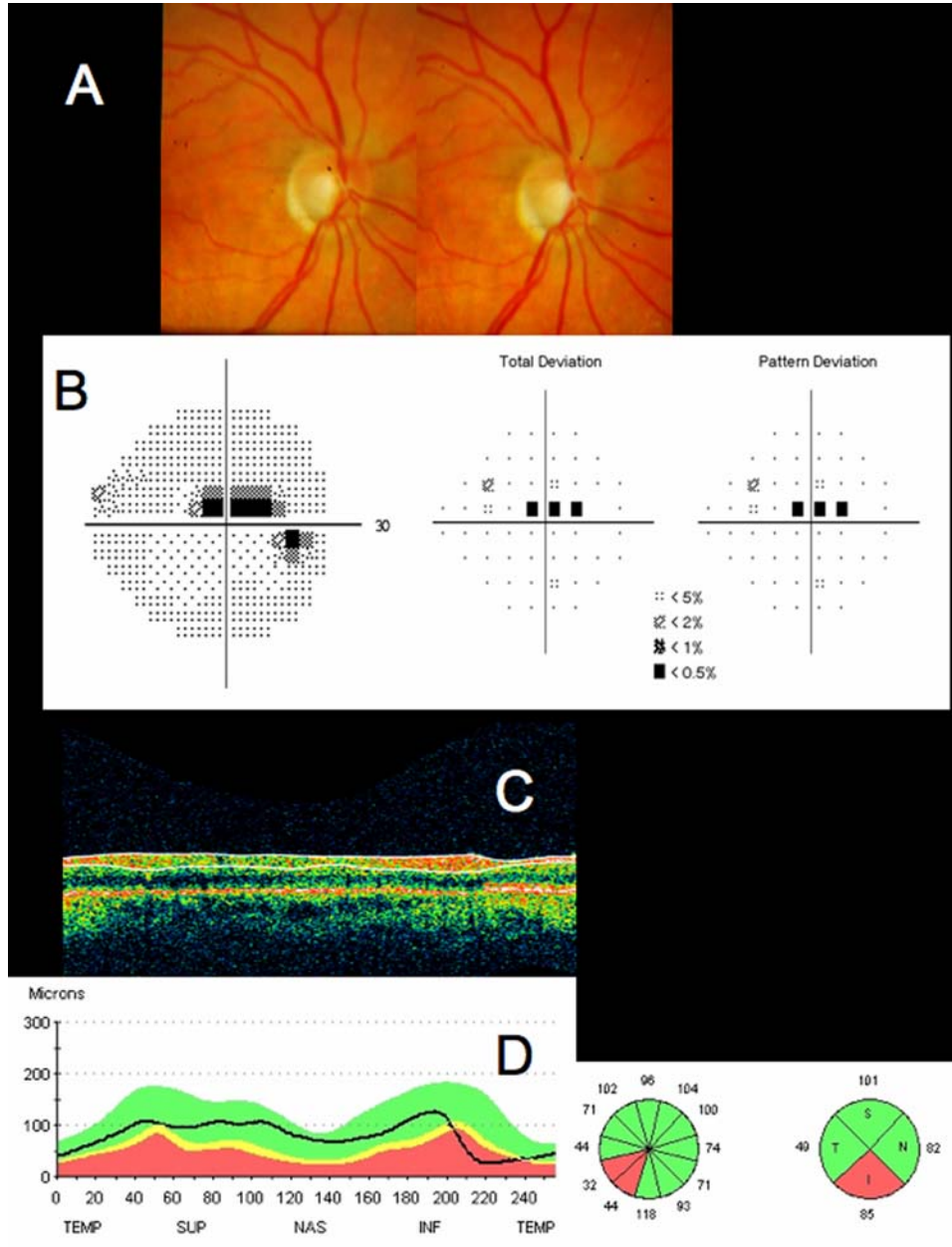


FIGURE 7

Optic nerve head (ONH) and retinal nerve fiber layer (RNFL) spectral domain optical coherence tomography (SD-OCT) images from healthy case study shown in Figures 5 and 6: A, Cirrus HD-OCT ONH 3D data set. Lower B-scan and upper B-scans are from position of blue and purple lines on the fundus view, respectively. B, RTVue ONH 3D data set. Upper left is en face image. Note vessel disconnect near top, indicating eye motion. Lower left and upper right B-scans are at the locations of the green and red lines on the en face image, respectively. 3D representation is at lower right. C, RTVue NHM4 scan pattern output. NHM4 is a pattern of radial scans combined with circular scans. Fundus view is in upper left. Radial B-scan and circular B-scan are indicated by red; white lines imposed over the RNFL thickness map represent other acquired scans. Warm colors in the map represent thick, healthy nerve fiber bundles. The 3.4-mm-diameter circle thickness graph and other parameter measurements are presented. D, RTVue RNFL scan pattern output. RNFL scan consists of four 3.4-mm-diameter circles around the ONH, whose RNFL segmentation thickness measurements are averaged. Sectorally averaged thicknesses are displayed in the round chart.



**FIGURE 8**

Standard clinical images from a patient with early glaucoma and a focal retinal nerve fiber layer (RNFL) defect. A, Stereoscopic disc photographs of right eye with inferotemporal defect, visible as marked cupping. B, Humphrey SITA 24-2 visual field threshold, total deviation, and pattern deviation maps, with superior paracentral scotoma. C, Time domain optical coherence tomography (TD-OCT) RNFL OCT scan. D, Comparison of TD-OCT RNFL thickness to normative database, with the inferior temporal RNFL thickness outside normal limits (red), consistent with visual field loss and optic nerve head loss of neuroretinal rim.

### Glaucoma Progression

One of the main benefits of ocular imaging is the ability to generate reproducible quantitative measurements, which can be compared over time for an individual subject in order to determine if the disease is progressing or if treatments are adequate. SD-OCT is able to give the high axial resolution and transverse scan density for these measurements, and acquisition of detailed 3D data sets that can be resampled for more accurate, reproducible measurements. The subject in this case study is a 49-year-old woman who displayed glaucomatous progression in both visual fields and RNFL thickness in her left eye between 2 visits 1 year apart. Visual field mean

deviation and pattern standard deviation progressed from  $-7.43$  dB and  $10.85$  dB, respectively, to  $-10.90$  dB and  $12.64$  dB, respectively, as the inferotemporal scotoma progressed superiorly and inferiorly (Figure 12). RNFL scans from the TD-OCT reveal some areas of possible change, such as in the inferior region, but possible circle placement changes between scans introduces artifact that makes comparison from visit to visit difficult (Figure 13A). SD-OCT RNFL measurements a year apart were able to be compared using RTVue commercial software (Figure 13C), which demonstrates RNFL thickness decrease globally, with the most loss superior-nasally, corresponding to the area of visual field loss. Overall progression can also be observed in the NHM4 scan (Figure 13D), where areas of green are being replaced by areas of blue. Some limited thinning over time can also be seen on the MM7 macular scan. On the MM7 scan, superior-inferior asymmetry actually decreases as the disease progresses, because one nerve fiber bundle had progressed first from the glaucoma, and as time passes, the tissue loss equalizes somewhat over the superior and inferior bundles. Tissue loss can also be observed in the 3D data sets, with deepening of the RNFL arcuate bundle loss troughs, especially superiorly, but inferiorly as well (Figure 13E).

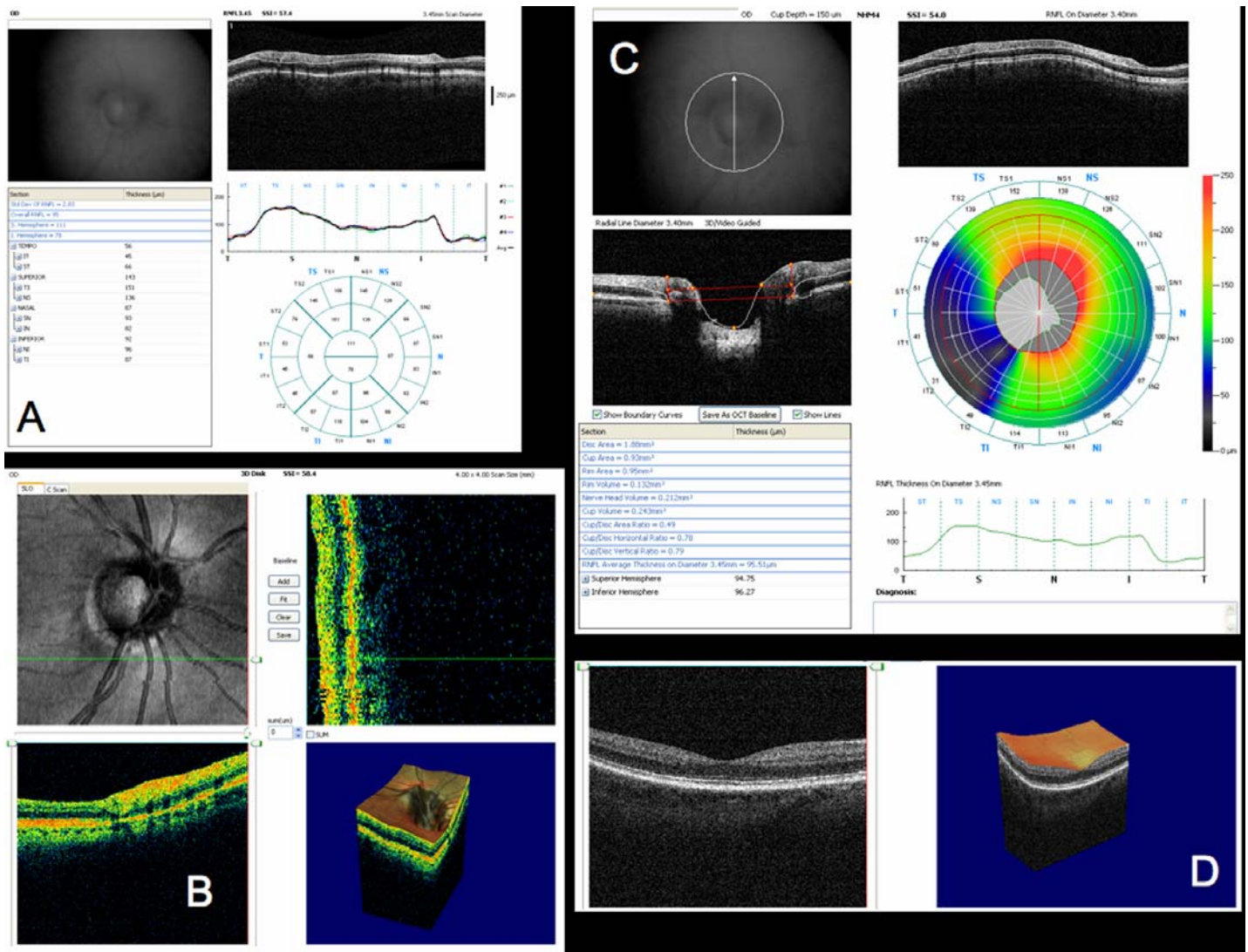


FIGURE 9

Spectral domain optical coherence tomography (SD-OCT) scans from the patient shown in Figure 8 with early glaucoma and a focal retinal nerve fiber layer (RNFL) defect. A, RTVue RNFL scan output. Note the clear inferior temporal notch, which can be more clearly measured without the oversmoothing problem of time domain OCT. B, RTVue 3D optical nerve head (ONH) 3D data set. Note how the tissue loss can be clearly seen in the B-scan obtained at the green line on the en face image, visible in the lower left corner. C, RTVue NHM4 scan output. Black and dark blue area inferior temporally indicates area of focal loss. The rest of the scan appears fairly healthy and thick. D, RTVue 3D data set from a macular scan, with 3D representation.

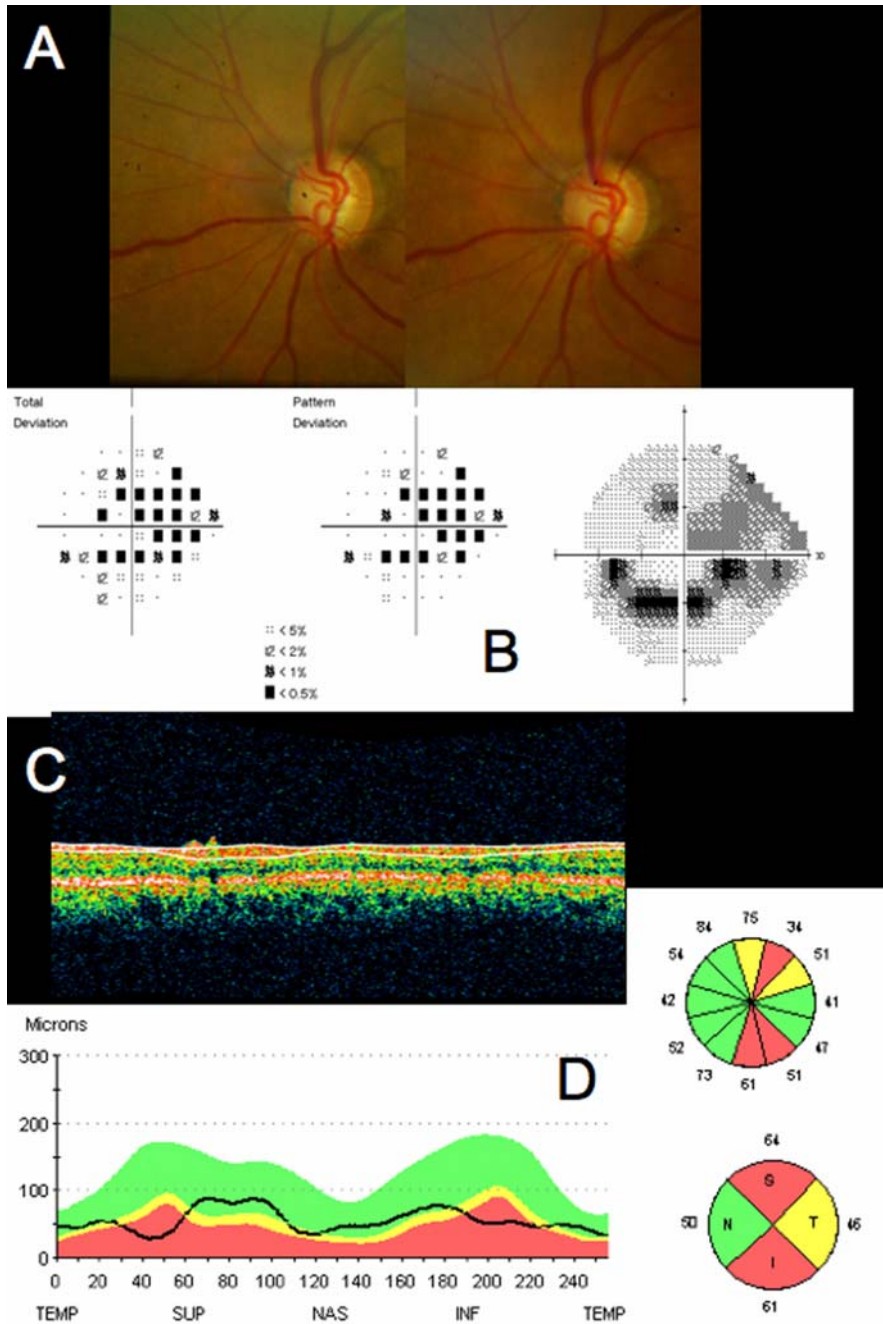


FIGURE 10

Standard clinical images from a patient with advanced glaucoma and global retinal nerve fiber layer (RNFL) and visual loss: A, Stereoscopic disc photograph showing overall neuroretinal rim loss in the optic disc, evidenced by marked optic nerve cupping. B, Humphrey SITA 24-2 visual field threshold, total deviation, and pattern deviation maps, with central inferior scotoma and temporal superior loss. C, Time domain optical coherence tomography RNFL scan, with RNFL thickness segmentation. Note slight segmentation error due to algorithm oversmoothing of the anterior RNFL tissue border superiorly. D, Comparison of RNFL thickness to normative database. RNFL loss results in nearly all areas showing thicknesses that are borderline or outside normal limits, except the nasal portion, where tissue loss typically appears last. The RNFL is markedly thin superiorly and inferiorly.

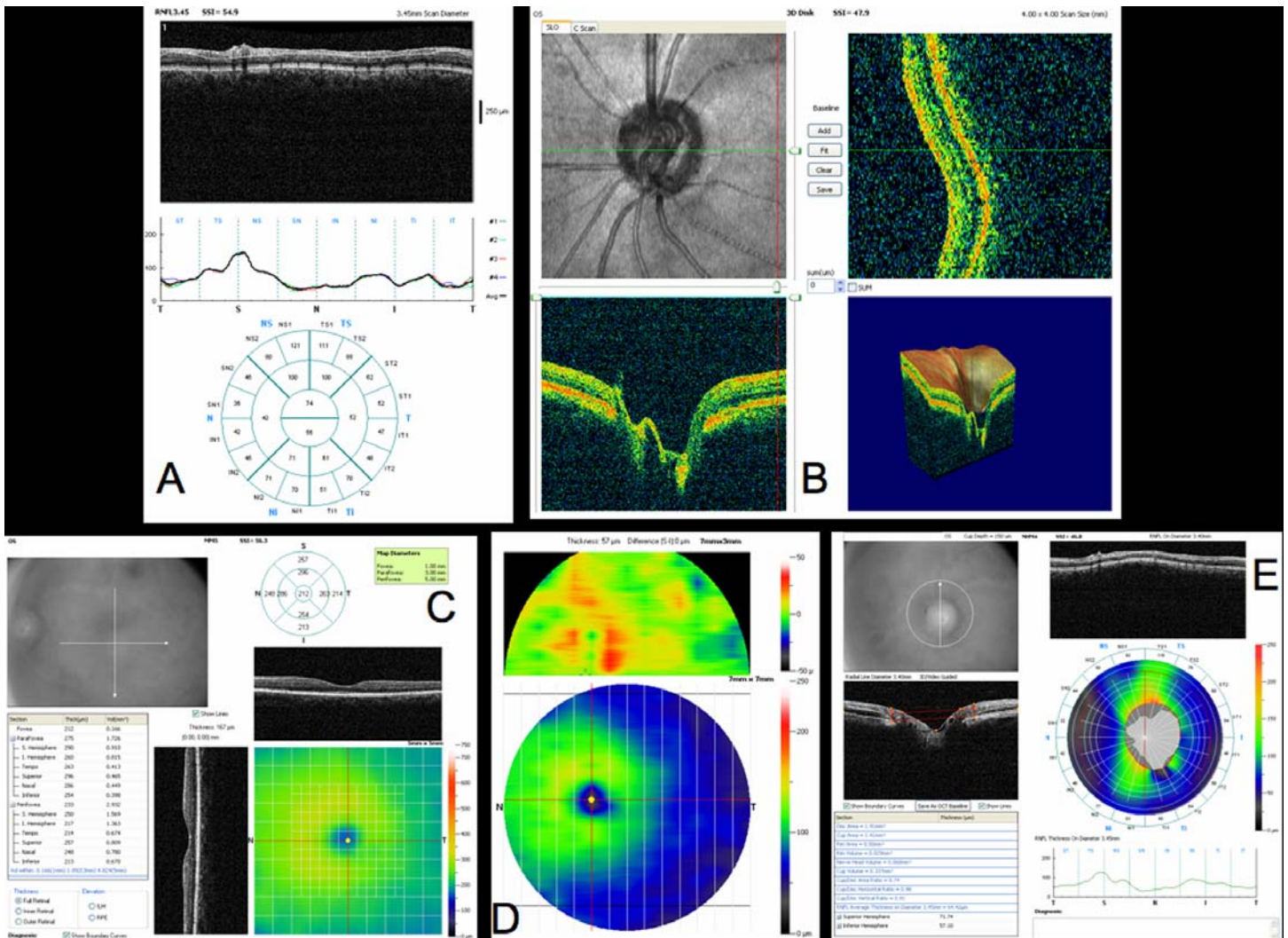


FIGURE 11

Spectral domain optical coherence tomography (SD-OCT) scans from the patient shown in Figure 10 with advanced glaucoma and global retinal nerve fiber layer (RNFL) and visual loss. A, RTVue RNFL scan output. Note the improved segmentation superiorly, compared to time-domain OCT (TD-OCT) in Figure 10C. B, RTVue optical nerve head (ONH) 3D data set, showing larger area of optic nerve cupping and thin neuroretinal rim. C, RTVue MM5 macular scan output, showing temporal thinning with advanced glaucoma. D, RTVue MM7 macular scan output, also showing temporal loss, and overall thinning. This figure shows inner retinal thickness specifically, using a relatively new segmentation algorithm that allows segmentation of the intraretinal layers beyond simply total retinal thickness and macular RNFL thickness. This algorithm also permits superior to inferior macular comparison by subtraction, as shown in the upper panel of Figure 11D. This demonstrates asymmetry in inner retinal thickness, with the inner retina thinner inferiorly than superiorly, consistent with the RNFL thickness shown in Figures 10 C and D and 11A and the visual field shown in Figure 10B. Note on the visual field (Figure 10B) that while there is perimetric damage both above and below the horizontal meridian, with a superior nasal defect and an inferior paracentral scotoma, the inferior defect is considerably deeper than the superior one, as borne out by the TD-OCT and SD-OCT. E, RTVue NHM4 scan output shows extensive RNFL thinning, with minimal areas represented with warm colors, and substantial black and dark blue areas.

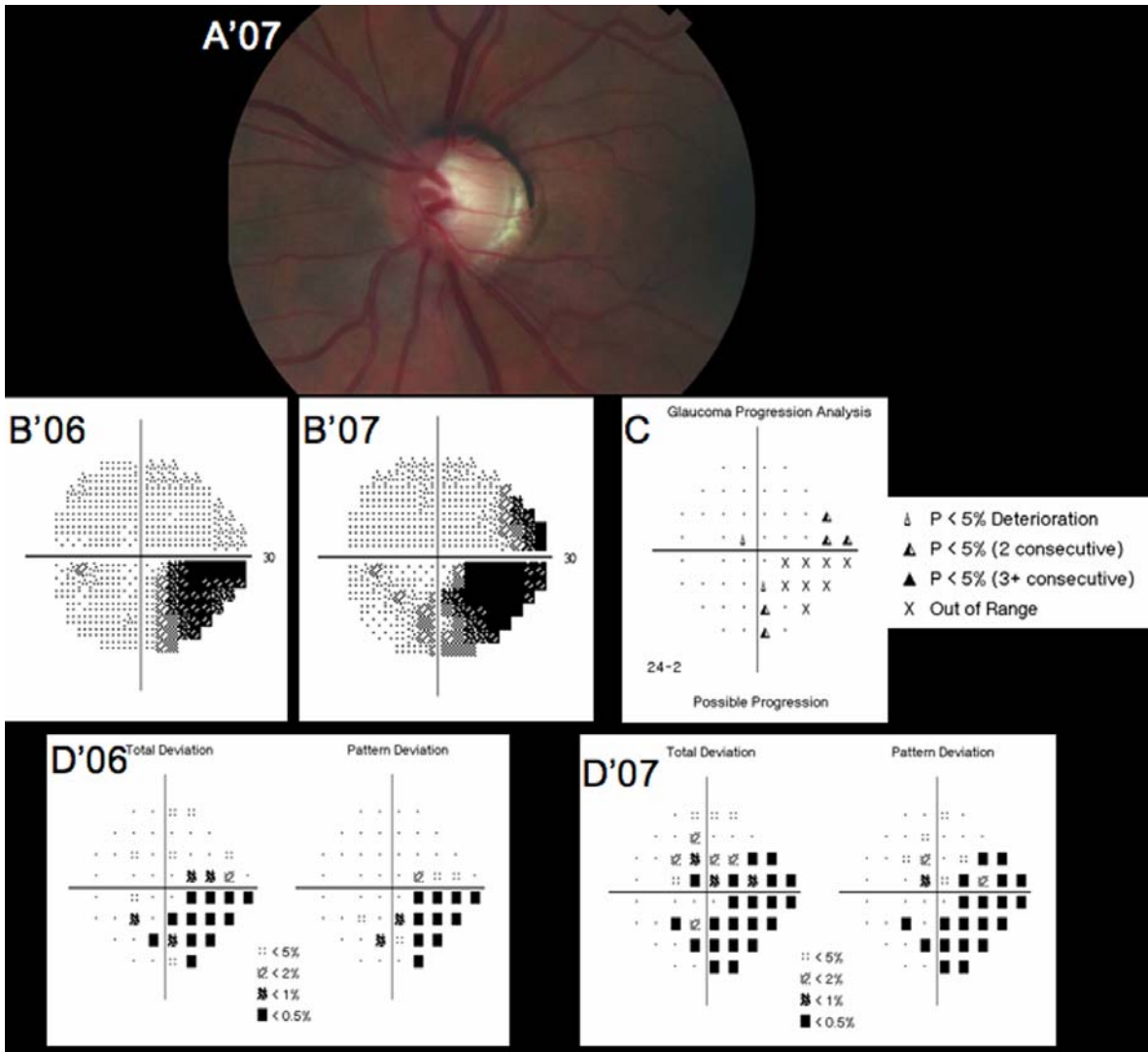


FIGURE 12

Standard clinical images from a patient with glaucoma progression. Two visits were a year apart: '06 denotes image from first visit, '07 denotes image from second visit. A, Disk photograph from second visit. Disc or fundus photography was not obtained at the first visit. B, Humphrey SITA 24-2 visual field threshold maps from first and second visit. C, Glaucoma progression analysis output between the two visits. Some inferior-temporal points were already too depressed to show progression, but significant progression occurred around the scotoma demonstrated at the first visit. D, Total and pattern deviation maps. These show similar progression to the other visual field analyses.

**Differentiating Glaucomatous Defects From Other Disease Effects: Differential Diagnosis**

In addition to identifying and tracking glaucomatous damage in cases where glaucoma is the only suspected disease, SD-OCT can be valuable in cases where differential diagnosis is needed between glaucoma and other retinal diseases. The subject of this case study is a 70-year-old white woman. IOP is in the normal range in both eyes, but she has a high cup-to-disc ratio in her right eye. She has a history of retinal tears treated with laser photocoagulation, cryotherapy, pars plana vitrectomy, and epiretinal membrane peeling in the right eye. She exhibited superior hemifield visual field loss in the right eye and a full visual field in her left eye. It was unknown based

on examination of fundus photography whether this right eye visual field defect was due to past retinal damage from the prior detachment or due to glaucomatous damage, requiring treatment for glaucoma (Figure 14). TD-OCT scans showed thin RNFL, but identification of the specific retinal layers affected remained somewhat unclear (Figure 14E, 14F). Comparison between the 2 eyes of retinal thicknesses near the macula using Cirrus 3D cube data sets shows the inner retinal thinning in the right eye, where the thinned area is represented by blue in the color map (Figure 15A, software of our own design). Shown B-scans are located near the top of each 3D cube raster scan. Scanning on Cirrus and Bioptigen SD-OCT devices revealed that the damage was isolated to the inner retinal layers, not the ones previously affected by the retinal detachment. This ability to identify the actual cellular layers where damage occurred makes possible the diagnosis of “glaucoma suspect,” with glaucoma as a high probability. While it is possible that inner retinal damage occurred as a result of this patient’s retinal detachment and surgeries, it is also possible that she has a chronic, progressive process, and deserves to be followed closely for any further inner retinal thinning (Figures 15C and D). All right eye SD-OCT scans show the roughness of the RNFL due to the loss, with a level of detail not visible on TD-OCT. Figure 15E shows the caliper measurements of the outer retina, demonstrating the similarity in outer retinal thickness in the affected and unaffected eyes.

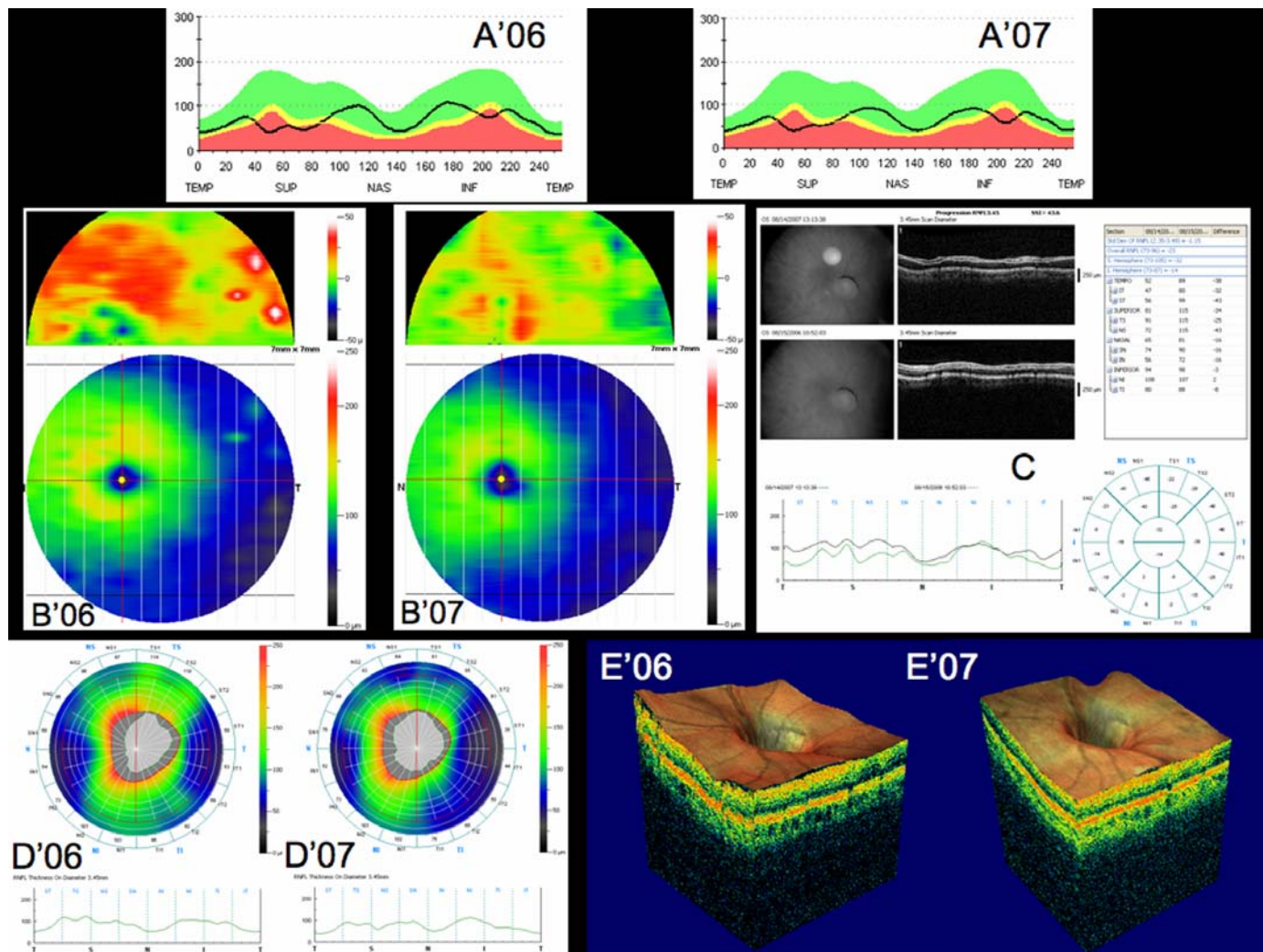
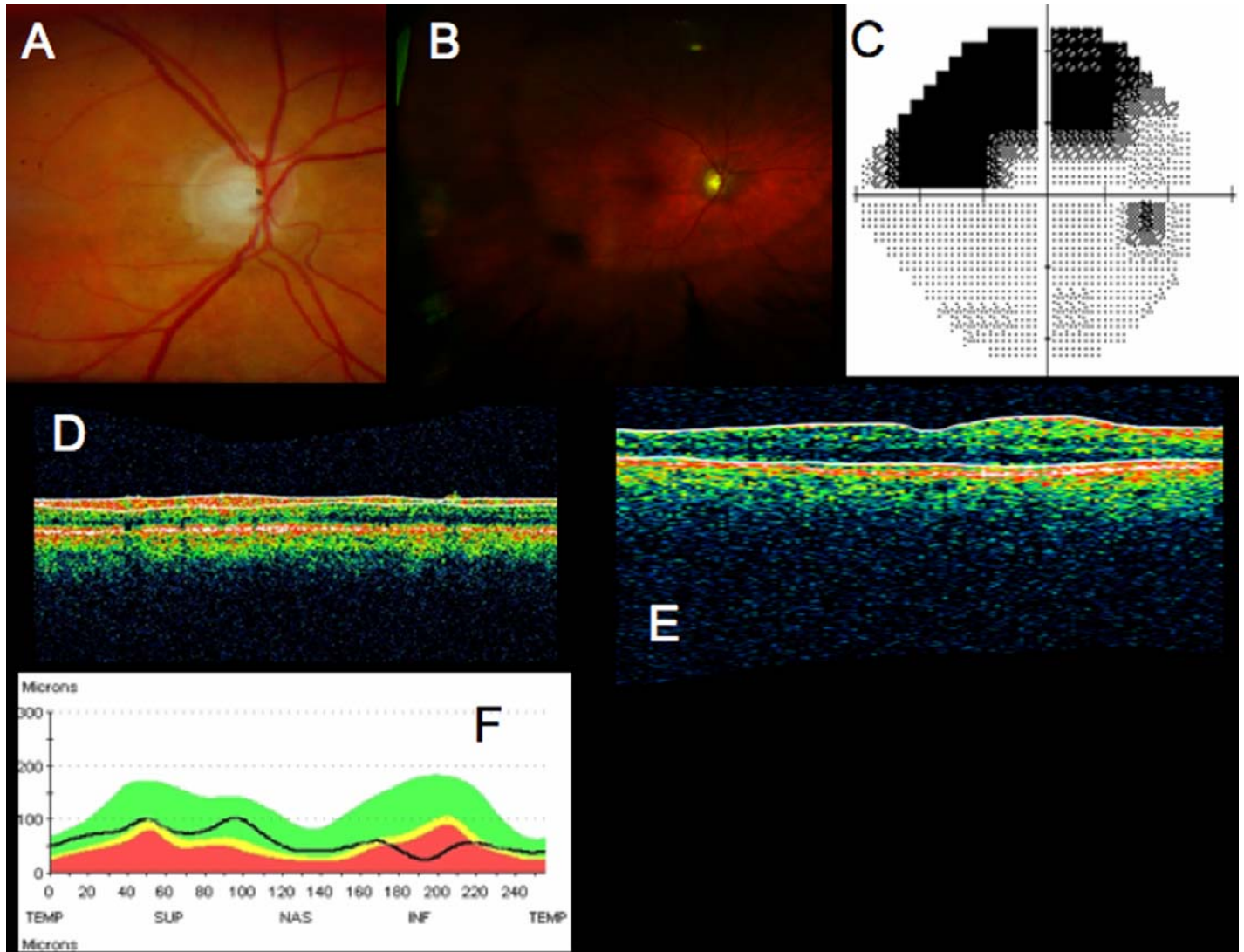


FIGURE 13

Optical coherence tomography (OCT) images from the patient in Figure 12 with glaucoma progression: Two visits were a year apart: '06 denotes image from first visit, '07 denotes image from second visit. A, Time-domain OCT retinal nerve fiber layer (RNFL) thicknesses compared to the normative database. Possible progression is shown inferiorly, but it is difficult to determine if appearance of progression is due to changes in 3.4-mm circle centration between scans. B, RTVue MM7 scans show overall macular scanning, with the superior hemisphere losing more tissue, bringing it more similar to the lower thickness of the inferior hemisphere. C, RTVue RNFL scans can be compared on its software to clearly show progression. RNFL thickness loss can be seen over nearly the entire circle, except inferior nasally. D, RTVue NHM4 RNFL thickness maps show loss overall, especially inferior temporally. E, RTVue optical nerve head (ONH) 3D data sets as 3D visualization also show increased cupping and RNFL tissue loss.



**FIGURE 14**

Standard clinical images from a patient with possible glaucoma: differential diagnosis case. A, Optic disc photograph from right eye. B, Optomap (Optos, Dunfermline, Scotland) fundus photograph showing peripheral retinal damage due to prior retinal detachment. Scarring is present around the closed retinal hole in the temporal periphery. C, Humphrey SITA 24-2 visual field threshold map showing superior temporal scotoma. D, Time domain optical coherence tomography (TD-OCT) RNFL imaging with segmentation. E, TD-OCT macular scan, showing a thin retina, but impossible to identify layers in which damage occurred. E, TD-OCT RNFL thickness comparison to normative database. Thinning is evident inferiorly, but depth location of thinning is not obvious.

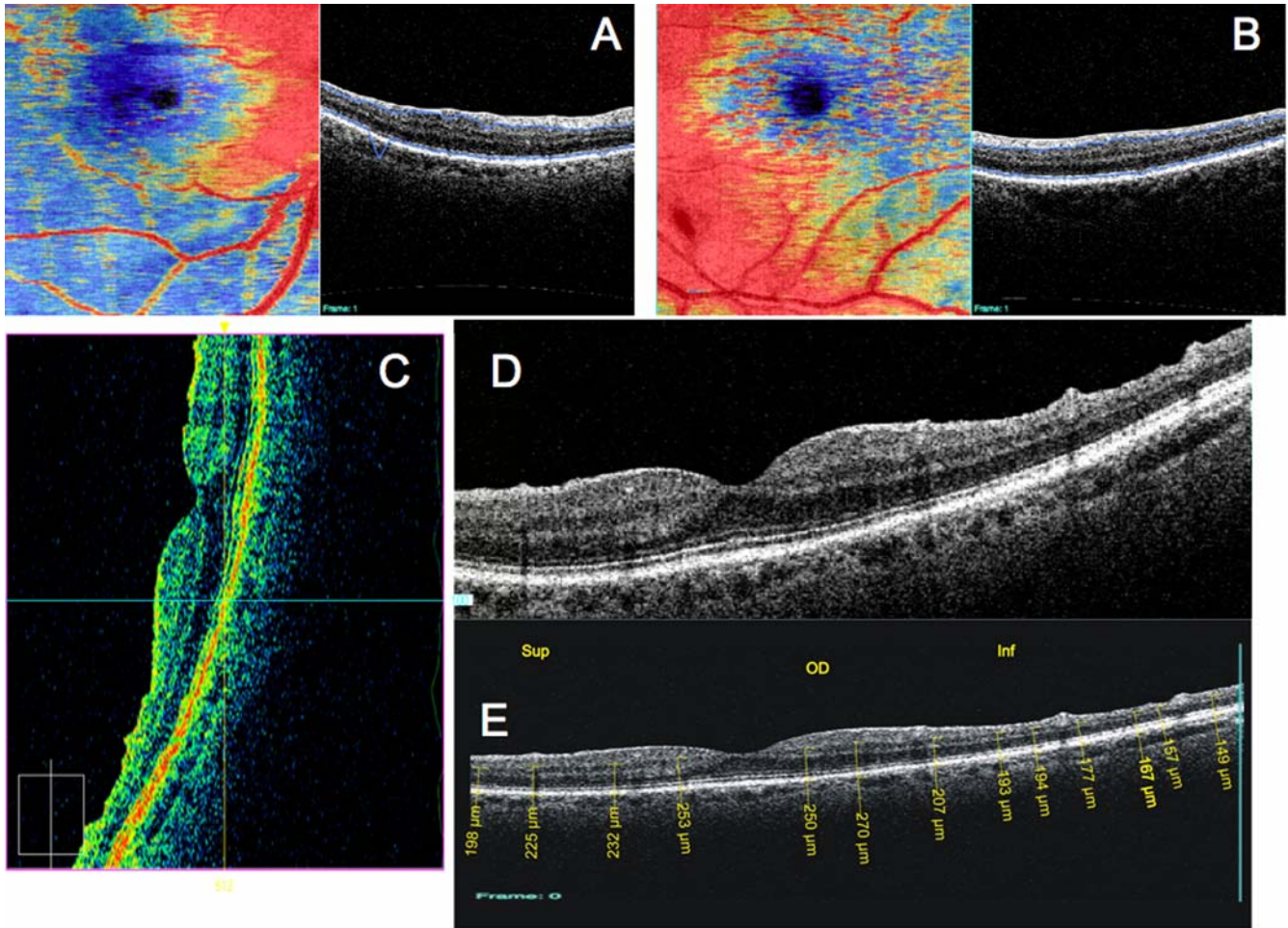


**FIGURE 15**

Spectral domain optical coherence tomography (SD-OCT) images from the patient in Figure 14 with possible glaucoma: differential diagnosis case: A and B, Total retinal thickness segmentation software of our own design on macular 3D data sets from the right eye and left eye, respectively. Macula is in the top half of each image. Retinal thickness loss is evident inferior to the macula in the right eye compared to the left eye (blue is thinner than red), but it is unknown in which layer this loss occurred without examining the SD-OCT B-scans. C, Vertical scan from a SD-OCT 3D data set taken with the macula in the superior half of the scan. Note the tissue loss is in the inner retina, including the retinal nerve fiber layer (RNFL), retinal ganglion cell layer, and inner plexiform layer, with outer retinal layers measuring and appearing no different between the patient's affected and unaffected eyes. D, Vertical OCT scan obtained by the Cirrus SD-OCT (left is the superior part of the scan, right is the inferior part of the scan). Retinal nerve fiber layer loss can be seen even more clearly in this scan, because of the device's higher axial resolution and transverse scan density compared to time domain OCT, where the disease has left the retina with an irregular-appearing surface. E, Same scan as D, with aspect ratio of 1:1 to allow manual calipers retinal layer thickness measurements to assess which cellular layers of the retina are damaged.

## DISCUSSION

To test reproducibility, mixed-effects models were used to find the variance in SD-OCT and TD-OCT, as well as compare them through the variance function, which is equal to TD-OCT variance divided by SD-OCT variance. If the variance of the 2 devices was equal, therefore, the variance function would be equal to 1, which is a valid conclusion statistically if the confidence interval for the variance function includes 1. Variance corresponds to the inverse of reproducibility: if a set of data from a certain device has a higher variance, there is more variability and the values that device provides are less reproducible.

For RNFL thickness, these models were calculated for global, quadrant, and clock hour measurements. Both SD-OCT and TD-OCT showed the most variability nasally out of the quadrants and in the nasally oriented clock hour 3. In general, clock hours tended to have greater variability, as is expected from data with a smaller sample size of points along the 3.4-mm circle. In comparing the 2 devices, global and nasal RNFLs were the only parameters to include 1 in the variance function confidence intervals. All other measurements' intervals were greater than 1, indicating TD-OCT displayed significantly more variability than SD-OCT in these sectors. Nasal RNFL barely contains 1 at the bottom of its confidence interval, so the larger amount of variability present in this sector in general may be affecting the ability to find a statistically significant difference between the 2 technologies in this sector. Global RNFL contains the most points acquired, so it is expected that both SD-OCT and TD-OCT would have this as the parameter with the lowest variance. Based on its confidence interval, there is no clear statistical difference between the 2 devices when measuring global RNFL. Perhaps in this TD-OCT data set, scanning circle position shifts, if present, were not excessive, resulting in no overall difference in global measurement, even if individual quadrant measurements were affected significantly. The axial resolution advantage that SD-OCT presents may also aid in getting more reproducible thickness measurements. These results clearly show that the method of marking the disc on a 3D data set and using that to calculate sectoral RNFL measurements can produce more reproducible, reliable data. These results are encouraging both in terms of standard TD-OCT's ability to provide reproducible, clinically useful data with regard to global RNFL thickness, and in terms of SD-OCT's statistically and clinically significant reduction in local variability. This suggests that SD-OCT may enable the use of more localized data, such as quadrants and clock hours, in determining glaucoma's presence or progression.

For macular total retinal thickness and RNFL thickness, the mixed-effects models were calculated globally, weighted for both SD-OCT and TD-OCT, and in the inner and outer sectors for total retinal thickness. Variability in the center 1-mm circle overlying the foveal depression varied by far the most out of any area on the scan, with variance at least 4 times greater than the next highest variance in each device. There are 2 factors that contribute to this variability. The first is decentration of the image. If the TD-OCT radial scans are not centered on the fovea, the averaged central thickness measured will be too thick, and whichever way the macula is shifted, that quadrant will measure artificially thin. This is also a problem for the SD-OCT measurements gathered in this study. Unlike the circular RNFL measurements, whose center was found based on an operator-traced disc margin, the center of the macula was not located by hand to centrally align it, so if the 3D scan was not centered, the macular thickness measurements also would not be centered properly. This would be an important modification to the future macular analysis software. The second cause of the much larger variability in the center sector is signal loss in the macula. Across the perimacular region, there is a thin but present RNFL, which substantially increases the reflectance of the surface of the retina; however, centrally in the fovea, this RNFL is absent, resulting in reduced reflectance, which affects the ability of segmentation software to properly identify the ILM at the retina's surface. This is relevant for both TD-OCT and SD-OCT, but based on subjective assessment of segmentation errors, the reduced resolution of TD-OCT actually helps its surface be more readily detectable in this case. This may be the reason TD-OCT presents a slightly lower variance than SD-OCT in the center sector, although the difference is not statistically significant.

The outer-sector SD-OCT measurements all displayed a significant improvement in reproducibility over their TD-OCT counterparts. This may be due to signal drop-off at the edges of the TD-OCT macular scans, causing underestimation of the retinal thickness. The inner temporal significant improvement in reproducibility of TD-OCT over SD-OCT is not expected. It may be that the fixation target where the patient focuses the eye while being scanned is placed differently in the SD-OCT than the TD-OCT, resulting in some sort of slight temporal displacement of the macula in the scanning frame, but it would be expected that this would shift the macula in all scans for an individual equally. The weighted mean retinal thickness, inner superior, and inner nasal sectors do show slight improvement in variance of SD-OCT over TD-OCT, but this difference is nonsignificant. Significant reproducibility improvements of the other sectors, as well as weighted mean RNFL thickness, may be due to SD-OCT's improved axial resolution. This is especially important for the variability of the measurement of the RNFL layer, since it is so much thinner than the overall retinal thickness, and the details of it as it thins toward the macula could be lost at poorer axial resolution of TD-OCT.

In the macular RNFL thickness reproducibility scans, the superior areas were affected in the fixed-effects model, with the macular inner and outer superior sectors measuring thicker on SD-OCT than TD-OCT, as well the center sector having a significantly thicker measurement on TD-OCT than on SD-OCT. The center differences can be explained by segmentation errors in the SD-OCT macular scans due to signal loss in the macular depression. Superior differences in thickness may be related to the interpolation required between the spokes of the radial scan in TD-OCT. The nerve fibers curve around the macula, and so the vertical radial line and the lines next to it that measure the superior thickness area may not slice through the nerve fibers at their thickest point, causing more of an impact when this underestimated value is interpolated between the line scans. For the RNFL, clock hours 8 and 12 had significantly larger TD-OCT measurements than SD-OCT. The reason this occurs only at these locations is unclear.

To test peripapillary RNFL thickness glaucoma discrimination, AUCs for SD-OCT and TD-OCT were compared. The confidence interval for the difference between them, TD-OCT minus SD-OCT, was found to contain zero for every global, quadrant, and clock hour sectoral parameter. This indicates that there is no statistically significant difference in the discrimination abilities of the 2 devices' peripapillary RNFL thicknesses. This is not entirely expected, because it would be expected that the significant improvement in RNFL SD-OCT reproducibility would also help improve discrimination. However, there are several factors that may be affecting this.

First, the SD-OCT devices tested here are not identical. The RTVue SD-OCT creates a 512×101 A-scan data set covering 4×4 mm. Cirrus SD-OCT was used to create a 200×200 A-scan data set covering 6×6 mm. Because of the difference in A-scan density, A-scan measurements are not quite the same density around the 3.4-mm circle, with A-scans closer together superiorly and inferiorly on the

SD-OCT circles. Unfortunately, we did not have a sufficient number of repeated same-day scans on the RTVue SD-OCT to create a reproducibility data set with this unit, or sufficient numbers of glaucoma patients scanned on the Cirrus SD-OCT to create a Cirrus discrimination data set that would have enough power to present meaningful results.

Segmentation software also performs differently on the 2 types of scans. Subjectively, RTVue SD-OCT scans appeared to be somewhat more variable in the quality of segmentation than Cirrus SD-OCT scans. This may be due to differences between the devices' scan appearance, if SD-OCT displays a wider range of reflectivities, making it easier for segmentation algorithms to detect boundaries between layers. However, SD-OCT segmentation results were observed to be sure there were no major errors in a particular scan, or it was removed from the data set.

Also, the glaucoma/healthy diagnosis was based solely on visual field assessment, so as not to bias it by testing structural elements with other structural elements. This probably results in lower AUCs for both TD-OCT and SD-OCT, because structural effects may not always correspond with visual defects. SD-OCT may be detecting slight glaucomatous loss with its higher resolution and less oversmoothed segmentation before visual field loss is occurring, and so the person was classified as healthy when that person actually has early disease. This is a problem in any clinically defined entity with no standard and consistent means for diagnosis and is especially true in glaucoma. In other words, SD-OCT identified "false positives" may actually have been perimetric "false negatives."

The comparison of RTVue SD-OCT and Stratus TD-OCT macular discrimination is made somewhat more complex because the 2 scans are not sampling the same tissue volume. SD-OCT macular 3D scans cover a 4-mm-wide area, whereas the TD-OCT scan samples out to 6 mm wide. Rather than adjusting for this difference by considering only the 4-mm central portion of the TD-OCT scan, to include the same tissue volume for both scans, it is a more fair comparison to make the discrimination based on all the information each device can provide about the macula, as long as it is noted that this is taken into consideration. By doing this, we are better assessing each device's true discrimination ability, rather than each device's ability to map a certain area of tissue.

Macular discrimination results were similar to peripapillary RNFL results, with nearly all parameters providing statistically similar discrimination abilities. RNFL weighted mean thickness values were the only ones with a statistically different discrimination value, with SD-OCT doing a significantly poorer job at identifying glaucoma cases. This is primarily due to segmentation failures. Subjectively, the SD-OCT macular RNFL boundaries were the most inconsistently segmented, with many scans being segmented to include portions of the ganglion cell layer in the thickness that was supposed to be only RNFL. This new segmentation software was known to have some reliability issues with segmentation of intraretinal layers, so we were initially unsure if it should be included in the analysis but decided it would be worthwhile to test its performance. On the basis of these results, RNFL thickness measurements from the SD-OCT should not be included in glaucoma assessment, since they provide not much better prediction abilities than random chance (AUC = 0.5).

As might be expected, central 1-mm-diameter macular/foveal measurements were also found to be essentially useless for glaucoma discrimination, with AUC not much better than random chance. This corresponds with their extremely poor reproducibility. While foveal thickness measurements are very helpful in cases of macular disease like macular holes or edema, they provide little information for determining glaucoma diagnosis.

Cases presented demonstrate the currently available clinical SD-OCT technology along with a few non-FDA-approved research devices of higher resolution. These cases are valuable in this thesis because they demonstrate the versatility that SD-OCT holds for making glaucoma diagnoses in cases of early, advanced, and progressing glaucoma, and differential diagnosis of glaucoma from other retinal diseases through physician clinical assessment. This is in addition to the quantitative glaucoma assessment of the thickness measurements tested in the reproducibility and discrimination portions of the study.

## **CONCLUSIONS**

---

Even at its current early stage of development, SD-OCT is able to demonstrate a statistically significant improvement in reproducibility in both peripapillary RNFL and macular scan thickness measurements over the clinical standard for TD-OCT. This improvement is primarily beneficial for sectoral measurements, not global measurements, making it especially important in the cases of focal loss of tissue, which occurs more often in the earlier stages of glaucoma. SD-OCT is able to perform as well at glaucoma discrimination as the current leading clinical TD-OCT device, and its performance is expected to improve as image processing and image analysis software progresses. SD-OCT also has significant clinical value for the subjective assessment of glaucoma, beyond the predictive values of individual output numbers.

It is perhaps surprising that SD-OCT is capable of outperforming the more mature TD-OCT in any way with so little image processing and image analysis software developed for SD-OCT to date. As indicated above, while even now SD-OCT offers rapid scan speeds and improved axial resolution compared to TD-OCT, software does not exist at this time to even begin to approach the potential power of SD-OCT. Specifically, the ability to perform 3D imaging with SD-OCT offers the opportunity to create OCT fundus images, permitting alignment and registration of images, and sampling of the exact same location on repeated visits. It will require additional technological innovation, particularly in the realm of image processing and analysis, to realize this technology's potential for structural imaging.

We have yet to take clinical advantage of the ability of SD-OCT to perform Doppler blood flow measurement (this is true blood flow, not velocity, since vessel caliber is known with this technology), oximetry, spectroscopic tissue biochemistry, or optophysiology. Finally, the scan acquisition speed has already been more than quadrupled in the laboratory through the use of new (and expensive) light sources. As these light sources become less expensive, more plentiful, and available in wavelengths conducive to high-resolution imaging, it is likely that SS-OCT will become the dominant technology, essentially producing an OCT camera capable

of real-time 3D OCT imaging.

## ACKNOWLEDGMENTS

Funding/Support: Supported in part by grants R01-EY013178-08 and P30-EY08098-21 from the National Institutes of Health, Bethesda, Maryland; the Eye and Ear Foundation, Pittsburgh, Pennsylvania; the Pittsburgh Foundation; and an unrestricted grant from Research to Prevent Blindness, Inc, New York, New York.

Financial Disclosures: The author receives royalties for intellectual property licensed by Massachusetts Institute of Technology to Carl Zeiss Meditec, Inc, and in the past 2 years has received research funding, research equipment, honoraria, and or payment of travel expenses from Alcon, Allergan, Heidelberg Engineering, Merck, and Optovue.

Conformity With Author Information: This study was approved by the Institutional Review Boards/Ethics Committee of the University of Pittsburgh, and adhered to the Declaration of Helsinki and Health Insurance Portability and Accountability Act regulations, with informed consent obtained from all subjects.

Other Acknowledgments: The author wishes to acknowledge Kelly A. Townsend, BS, for assistance in study design and conduct, data collection and management, data interpretation, and manuscript preparation, review, and approval; Hiroshi Ishikawa, MD, for data analysis; Jongsick Kim, BS, for data analysis; Gadi Wollstein, MD, for study design and conduct, data analysis, and data interpretation; and Richard A. Bilonick, PhD, for statistical assistance. All are from the UPMC Eye Center, Eye and Ear Institute, Ophthalmology and Visual Science Research Center, Department of Ophthalmology, University of Pittsburgh School of Medicine, Pittsburgh, Pennsylvania, and Dr. Ishikawa and Mr. Kim are also with the Department of Bioengineering, Swanson School of Engineering, University of Pittsburgh, Pittsburgh, Pennsylvania.

## REFERENCES

1. de Boer JF, Cense B, Park BH, Pierce MC, Tearney GJ, Bouma BE. Improved signal-to-noise ratio in spectral-domain compared with time-domain optical coherence tomography. *Opt Lett* 2003;28:2067-2069.
2. Drexler W, Morgner U, Ghanta RK, Kartner FX, Schuman JS, Fujimoto JG. Ultrahigh-resolution ophthalmic optical coherence tomography. *Nat Med* 2001;7:502-507.
3. Drexler W, Sattmann H, Hermann B, et al. Enhanced visualization of macular pathology with the use of ultrahigh-resolution optical coherence tomography. *Arch Ophthalmol* 2003;121:695-706.
4. Fujimoto JG. Optical coherence tomography for ultrahigh resolution in vivo imaging. *Nat Biotechnol* 2003;21:1361-1367.
5. Fujimoto JG, Pitris C, Boppart SA, Brezinski ME. Optical coherence tomography: an emerging technology for biomedical imaging and optical biopsy. *Neoplasia* 2000;2:9-25.
6. Hee MR, Izatt JA, Swanson EA, et al. Optical coherence tomography of the human retina. *Arch Ophthalmol* 1995;113:325-332.
7. Ko TH, Fujimoto JG, Schuman JS, et al. Comparison of ultrahigh- and standard-resolution optical coherence tomography for imaging macular pathology. *Ophthalmology* 2005;112:1922.e1-15.
8. Wojtkowski M, Srinivasan V, Fujimoto JG, et al. Three-dimensional retinal imaging with high-speed ultrahigh-resolution optical coherence tomography. *Ophthalmology* 2005;112:1734-1746.
9. Wojtkowski M, Srinivasan V, Ko T, Fujimoto JG, Kowalczyk A, Duker J. Ultrahigh-resolution, high-speed, Fourier domain optical coherence tomography and methods for dispersion compensation. *Optics Express* 2004;12:2404-2422.
10. Wollstein G, Paunescu LA, Ko TH, et al. Ultrahigh-resolution optical coherence tomography in glaucoma. *Ophthalmology* 2005;112:229-237.
11. Gabriele ML, Ishikawa H, Wollstein G, et al. Peripapillary nerve fiber layer thickness profile determined with high speed, ultrahigh resolution optical coherence tomography high-density scanning. *Invest Ophthalmol Vis Sci* 2007;48:3154-3160.
12. Anger EM, Unterhuber A, Hermann B, et al. Ultrahigh resolution optical coherence tomography of the monkey fovea. Identification of retinal sublayers by correlation with semithin histology sections. *Exp Eye Res* 2004;78:1117-1125.
13. Nassif N, Cense B, Park BH, et al. In vivo human retinal imaging by ultrahigh-speed spectral domain optical coherence tomography. *Opt Lett* 2004;29:480-482.
14. Scholda C, Wirtitsch M, Hermann B, et al. Ultrahigh resolution optical coherence tomography of macular holes. *Retina* 2006;26:1034-1041.
15. Ko TH, Witkin AJ, Fujimoto JG, et al. Ultrahigh-resolution optical coherence tomography of surgically closed macular holes. *Arch Ophthalmol* 2006;124:827-836.
16. Wirtitsch MG, Ergun E, Hermann B, et al. Ultrahigh resolution optical coherence tomography in macular dystrophy. *Am J Ophthalmol* 2005;140:976-983.
17. Paunescu LA, Ko TH, Duker JS, et al. Idiopathic juxtafoveal retinal telangiectasis: new findings by ultrahigh-resolution optical coherence tomography. *Ophthalmology* 2006;113:48-57.
18. Schmidt-Erfurth U, Leitgeb RA, Michels S, et al. Three-dimensional ultrahigh-resolution optical coherence tomography of macular diseases. *Invest Ophthalmol Vis Sci* 2005;46:3393-3402.
19. Gloesmann M, Hermann B, Schubert C, Sattmann H, Ahnelt PK, Drexler W. Histologic correlation of pig retina radial stratification with ultrahigh-resolution optical coherence tomography. *Invest Ophthalmol Vis Sci* 2003;44:1696-1703.

20. Wojtkowski M, Leitgeb R, Kowalczyk A, Bajraszewski T, Fercher AF. In vivo human retinal imaging by Fourier domain optical coherence tomography. *J Biomed Opt* 2002;7:457-463.
21. Chan A, Duker JS, Ishikawa H, Ko TH, Schuman JS, Fujimoto JG. Quantification of photoreceptor layer thickness in normal eyes using optical coherence tomography. *Retina* 2006;26:655-660.
22. Ko TH, Fujimoto JG, Duker JS, et al. Comparison of ultrahigh- and standard-resolution optical coherence tomography for imaging macular hole pathology and repair. *Ophthalmology* 2004;111:2033-2043.
23. Srinivasan VJ, Wojtkowski M, Witkin AJ, et al. High-definition and 3-dimensional imaging of macular pathologies with high-speed ultrahigh-resolution optical coherence tomography. *Ophthalmology* 2006;113:2054.e1-14.
24. Kaushik S, Gyatsho J, Jain R, Pandav SS, Gupta A. Correlation between retinal nerve fiber layer thickness and central corneal thickness in patients with ocular hypertension: an optical coherence tomography study. *Am J Ophthalmol* 2006;141:884-890.
25. Leung CK, Mohamed S, Leung KS, et al. Retinal nerve fiber layer measurements in myopia: an optical coherence tomography study. *Invest Ophthalmol Vis Sci* 2006;47:5171-5176.
26. Drexler W, Fujimoto JG. State-of-the-art retinal optical coherence tomography. *Prog Ret Eye Res* 2008;27:45-88.
27. Srinivasan VJ, Huber R, Gorczynska I, et al. High-speed, high-resolution optical coherence tomography retinal imaging with a frequency-swept laser at 850 nm. *Opt Lett* 2007;32:361-363.
28. Lim H, Mujat M, Kerbage C, et al. High-speed imaging of human retina in vivo with swept-source optical coherence tomography. *Optics Express* 2006;14:12902-12908.
29. Schuman JS, Hee MR, Arya AV, et al. Optical coherence tomography: a new tool for glaucoma diagnosis. *Curr Opin Ophthalmol* 1995;6:89-95.
30. Puliafito CA, Hee MR, Lin CP, et al. Imaging of macular diseases with optical coherence tomography. *Ophthalmology* 1995;102:217-229.
31. Wollstein G, Ishikawa H, Wang J, Beaton SA, Schuman JS. Comparison of three optical coherence tomography scanning areas for detection of glaucomatous damage. *Am J Ophthalmol* 2005;139:39-43.
32. Christopoulos V, Kagemann L, Wollstein G, et al. In vivo corneal high-speed, ultra high-resolution optical coherence tomography. *Arch Ophthalmol* 2007;125:1027-1035.
33. Izatt JA, Hee MR, Swanson EA, et al. Micrometer-scale resolution imaging of the anterior eye in vivo with optical coherence tomography. *Arch Ophthalmol* 1994;112:1584-1589.
34. Konstantopoulos A, Hossain P, Anderson DF. Recent advances in ophthalmic anterior segment imaging: a new era for ophthalmic diagnosis? *Br J Ophthalmol* 2007;91:551-557.
35. Mohamed S, Lee GK, Rao SK, et al. Repeatability and reproducibility of pachymetric mapping with visante anterior segment optical coherence tomography. *Invest Ophthalmol Vis Sci* 2007;48:5499-5504.
36. Hsiung PL, Phatak DR, Chen Y, Aguirre AD, Fujimoto JG, Connolly JL. Benign and malignant lesions in the human breast depicted with ultrahigh resolution and three-dimensional optical coherence tomography. *Radiology* 2007;244:865-874.
37. Chen Y, Andrews PM, Aguirre AD, Schmitt JM, Fujimoto JG. High-resolution three-dimensional optical coherence tomography imaging of kidney microanatomy ex vivo. *J Biomed Opt* 2007;12:034008.
38. Cobb MJ, Chen Y, Underwood RA, Usui ML, Olerud J, Li X. Noninvasive assessment of cutaneous wound healing using ultrahigh-resolution optical coherence tomography. *J Biomed Opt* 2006;11:064002.
39. de Giorgi V, Stante M, Massi D, Mavilia L, Cappugi P, Carli P. Possible histopathologic correlates of dermoscopic features in pigmented melanocytic lesions identified by means of optical coherence tomography. *Exp Dermatol* 2005;14:56-59.
40. Gambichler T, Regeniter P, Bechara FG, et al. Characterization of benign and malignant melanocytic skin lesions using optical coherence tomography in vivo. *J Am Acad Dermatol* 2007;57:629-637.
41. Olmedo JM, Warschaw KE, Schmitt JM, Swanson DL. Optical coherence tomography for the characterization of basal cell carcinoma in vivo: a pilot study. *J Am Acad Dermatol* 2006;55:408-412.
42. Pierce MC, Strasswimmer J, Park BH, Cense B, de Boer JF. Advances in optical coherence tomography imaging for dermatology. *J Invest Dermatol* 2004;123:458-463.
43. Singer AJ, Wang Z, McClain SA, Pan Y. Optical coherence tomography: a noninvasive method to assess wound reepithelialization. *Acad Emerg Med* 2007;14:387-391.
44. Huang D, Swanson EA, Lin CP, et al. Optical coherence tomography. *Science* 1991;254:1178-1181.
45. Fercher AF, Hitzinger CK, Drexler W, Kamp G, Sattmann H. In vivo optical coherence tomography. *Am J Ophthalmol* 1993;116:113-114.
46. Drexler W. Ultrahigh-resolution optical coherence tomography. *J Biomed Opt* 2004;9:47-74.
47. Wojtkowski M. Phase sensitive interferometry in optical coherence tomography. *Proc SPIE* 2001;4515.
48. Baikoff G. Anterior segment OCT and phakic intraocular lenses: a perspective. *J Cataract Refract Surg* 2006;32:1827-1835.
49. Bohringer HJ, Lankenau E, Rohde V, Huttmann G, Giese A. Optical coherence tomography for experimental neuroendoscopy. *Minim Invasive Neurosurg* 2006;49:269-275.
50. Brezinski ME, Tearney GJ, Boppart SA, Swanson EA, Southern JF, Fujimoto JG. Optical biopsy with optical coherence tomography: feasibility for surgical diagnostics. *J Surg Res* 1997;71:32-40.
51. Brezinski ME, Tearney GJ, Bouma BE, et al. Optical coherence tomography for optical biopsy. Properties and demonstration of vascular pathology. *Circulation* 1996;93:1206-1213.

52. Chia S, Christopher Raffel O, Takano M, Tearney GJ, Bouma BE, Jang IK. In-vivo comparison of coronary plaque characteristics using optical coherence tomography in women vs. men with acute coronary syndrome. *Coron Artery Dis* 2007;18:423-427.
53. Raffel OC, Tearney GJ, Gauthier DD, Halpern EF, Bouma BE, Jang IK. Relationship between a systemic inflammatory marker, plaque inflammation, and plaque characteristics determined by intravascular optical coherence tomography. *Arterioscler Thromb Vasc Biol* 2007;27:1820-1827.
54. Bower BA, Zhao M, Zawadzki RJ, Izatt JA. Real-time spectral domain Doppler optical coherence tomography and investigation of human retinal vessel autoregulation. *J Biomed Opt* 2007;12:041214.
55. Leitgeb RA, Schmetterer L, Hitzinger CK, et al. Real-time measurement of in vitro flow by Fourier-domain color Doppler optical coherence tomography. *Opt Lett* 2004;29:171-173.
56. Wang Y, Bower BA, Izatt JA, Tan O, Huang D. In vivo total retinal blood flow measurement by Fourier domain Doppler optical coherence tomography. *J Biomed Opt* 2007;12:041215.
57. Yazdanfar S, Rollins AM, Izatt JA. In vivo imaging of human retinal flow dynamics by color Doppler optical coherence tomography. *Arch Ophthalmol* 2003;121:235-239.
58. Kagemann L, Wollstein G, Wojtkowski M, et al. Spectral oximetry assessed with high-speed ultra-high-resolution optical coherence tomography. *J Biomed Opt* 2007;12:041212.
59. Bizheva K, Pflug R, Hermann B, et al. Otophysiology: depth-resolved probing of retinal physiology with functional ultrahigh-resolution optical coherence tomography. *Proc Natl Acad Sci U S A* 2006;103:5066-5071.
60. Srinivasan VJ, Wojtkowski M, Fujimoto JG, Duker JS. In vivo measurement of retinal physiology with high-speed ultrahigh-resolution optical coherence tomography. *Opt Lett* 2006;31:2308-2310.
61. Zhang J, Rao B, Chen Z. Swept source based fourier domain functional optical coherence tomography. *Conf Proc IEEE Eng Med Biol Soc* 2005;7:7230-7233.
62. Hewick SA, Fairhead AC, Culy JC, Atta HR. A comparison of 10 MHz and 20 MHz ultrasound probes in imaging the eye and orbit. *Br J Ophthalmol* 2004;88:551-555.
63. Fujimoto JG, Brezinski ME, Tearney GJ, et al. Optical biopsy and imaging using optical coherence tomography. *Nat Med* 1995;1:970-972.
64. Jorgensen TM, Thomadsen J, Christensen U, Soliman W, Sander B. Enhancing the signal-to-noise ratio in ophthalmic optical coherence tomography by image registration—method and clinical examples. *J Biomed Opt* 2007;12:041208.
65. Ishikawa H, Piette S, Liebmann JM, Ritch R. Detecting the inner and outer borders of the retinal nerve fiber layer using optical coherence tomography. *Graefes Arch Clin Exp Ophthalmol* 2002;40:362-371.
66. Ishikawa H, Stein DM, Wollstein G, Beaton S, Fujimoto JG, Schuman JS. Macular segmentation with optical coherence tomography. *Invest Ophthalmol Vis Sci* 2005;46:2012-2017.
67. Sommer A, Katz J, Quigley HA, et al. Clinically detectable nerve fiber atrophy precedes the onset of glaucomatous field loss. *Arch Ophthalmol* 1991;109:77-83.
68. Schuman JS, Pedut-Kloizman T, Hertzmark E, et al. Reproducibility of nerve fiber layer thickness measurements using optical coherence tomography. *Ophthalmology* 1996;103:1889-1898.
69. Quigley HA, Katz J, Derick RJ, Gilbert D, Sommer A. An evaluation of optic disc and nerve fiber layer examinations in monitoring progression of early glaucoma damage. *Ophthalmology* 1992;99:19-28.
70. Sommer A, Miller NR, Pollack I, Maumenee AE, George T. The nerve fiber layer in the diagnosis of glaucoma. *Arch Ophthalmol* 1977;95:2149-2156.
71. Medeiros FA, Zangwill LM, Bowd C, Sample PA, Weinreb RN. Use of progressive glaucomatous optic disk change as the reference standard for evaluation of diagnostic tests in glaucoma. *Am J Ophthalmol* 2005;139:1010-1018.
72. Harwerth RS, Carter-Dawson L, Shen F, Smith EL 3rd, Crawford ML. Ganglion cell losses underlying visual field defects from experimental glaucoma. *Invest Ophthalmol Vis Sci* 1999;40:2242-2250.
73. Bengtsson B, Heijl A. A long-term prospective study of risk factors for glaucomatous visual field loss in patients with ocular hypertension. *J Glaucoma* 2005;14:135-138.
74. Gordon MO, Beiser JA, Brandt JD, et al. The Ocular Hypertension Treatment Study: baseline factors that predict the onset of primary open-angle glaucoma. *Arch Ophthalmol* 2002;120:714-720; discussion 829-730.
75. Medeiros FA, Sample PA, Zangwill LM, Bowd C, Aihara M, Weinreb RN. Corneal thickness as a risk factor for visual field loss in patients with preperimetric glaucomatous optic neuropathy. *Am J Ophthalmol* 2003;136:805-813.
76. Gupta N, Ly T, Zhang Q, Kaufman PL, Weinreb RN, Yucel YH. Chronic ocular hypertension induces dendrite pathology in the lateral geniculate nucleus of the brain. *Exp Eye Res* 2007;84:176-184.
77. Gupta N, Yucel YH. Glaucoma as a neurodegenerative disease. *Curr Opin Ophthalmol* 2007;18:110-114.
78. Sigal IA, Flanagan JG, Tertinegg I, Ethier CR. Predicted extension, compression and shearing of optic nerve head tissues. *Exp Eye Res* 2007;85:312-322.
79. Yang H, Downs JC, Girkin C, et al. 3-D histomorphometry of the normal and early glaucomatous monkey optic nerve head: lamina cribrosa and peripapillary scleral position and thickness. *Invest Ophthalmol Vis Sci* 2007;48:4597-4607.
80. Yucel YH, Zhang Q, Gupta N, Kaufman PL, Weinreb RN. Loss of neurons in magnocellular and parvocellular layers of the lateral geniculate nucleus in glaucoma. *Arch Ophthalmol* 2000;118:378-384.

81. Yucel YH, Zhang Q, Weinreb RN, Kaufman PL, Gupta N. Atrophy of relay neurons in magno- and parvocellular layers in the lateral geniculate nucleus in experimental glaucoma. *Invest Ophthalmol Vis Sci* 2001;42:3216-3222.
82. Yucel YH, Zhang Q, Weinreb RN, Kaufman PL, Gupta N. Effects of retinal ganglion cell loss on magno-, parvo-, koniocellular pathways in the lateral geniculate nucleus and visual cortex in glaucoma. *Prog Retin Eye Res* 2003;22:465-481.
83. Badala F, Nouri-Mahdavi K, Raoof DA, Leeprechanon N, Law SK, Caprioli J. Optic disk and nerve fiber layer imaging to detect glaucoma. *Am J Ophthalmol* 2007;144:724-732.
84. Budenz DL, Fredette MJ, Feuer WJ, Anderson DR. Reproducibility of peripapillary retinal nerve fiber thickness measurements with Stratus OCT in glaucomatous eyes. *Ophthalmology* 2008;115:661-666.
85. Hougaard JL, Heijl A, Bengtsson B. Glaucoma detection by Stratus OCT. *J Glaucoma* 2007;16:302-306.
86. Wollstein G, Schuman JS, Price LL, et al. Optical coherence tomography longitudinal evaluation of retinal nerve fiber layer thickness in glaucoma. *Arch Ophthalmol* 2005;123:464-470.
87. Paunescu LA, Schuman JS, Price LL, et al. Reproducibility of nerve fiber thickness, macular thickness, and optic nerve head measurements using StratusOCT. *Invest Ophthalmol Vis Sci* 2004;45:1716-1724.
88. Schuman JS, Puliafito CA, Fujimoto JG. *Everyday OCT: A Handbook for Clinicians and Technicians*. Thorofare, NJ: Slack, Inc; 2006.
89. Stein DM, Wollstein G, Ishikawa H, Hertzmark E, Noecker RJ, Schuman JS. Effect of corneal drying on optical coherence tomography. *Ophthalmology* 2006;113:985-991.
90. Leitgeb R, Wojtkowski M, Kowalczyk A, Hitztenberger CK, Sticker M, Fercher AF. Spectral measurement of absorption by spectroscopic frequency-domain optical coherence tomography. *Opt Lett* 2000;25:820-822.
91. Li Q, Timmers AM, Hunter K, et al. Noninvasive imaging by optical coherence tomography to monitor retinal degeneration in the mouse. *Invest Ophthalmol Vis Sci* 2001;42:2981-2989.
92. Srinivasan VJ, Ko TH, Wojtkowski M, et al. Noninvasive volumetric imaging and morphometry of the rodent retina with high-speed, ultrahigh-resolution optical coherence tomography. *Invest Ophthalmol Vis Sci* 2006;47:5522-5528.
93. Choma MA, Hsu K, Izatt JA. Swept source optical coherence tomography using an all-fiber 1300-nm ring laser source. *J Biomed Opt* 2005;10:44009.
94. Huber R, Adler DC, Fujimoto JG. Buffered Fourier domain mode locking: unidirectional swept laser sources for optical coherence tomography imaging at 370,000 lines/s. *Opt Lett* 2006;31:2975-2977.
95. Liu B, Brezinski ME. Theoretical and practical considerations on detection performance of time domain, Fourier domain, and swept source optical coherence tomography. *J Biomed Opt* 2007;12:044007.
96. Fernandez EJ, Povazay B, Hermann B, et al. Three-dimensional adaptive optics ultrahigh-resolution optical coherence tomography using a liquid crystal spatial light modulator. *Vision Res* 2005;45:3432-3444.
97. Hermann B, Fernandez EJ, Unterhuber A, et al. Adaptive-optics ultrahigh-resolution optical coherence tomography. *Opt Lett* 2004;29:2142-2144.
98. Liang J, Williams DR, Miller DT. Supernormal vision and high-resolution retinal imaging through adaptive optics. *J Opt Soc Am A Opt Image Sci Vis* 1997;14:2884-2892.
99. Roorda A, Williams DR. The arrangement of the three cone classes in the living human eye. *Nature* 1999;397:520-522.
100. Vilupuru AS, Rangaswamy NV, Frishman LJ, Smith EL 3rd, Harwerth RS, Roorda A. Adaptive optics scanning laser ophthalmoscopy for in vivo imaging of lamina cribrosa. *J Opt Soc Am A Opt Image Sci Vis* 2007;24:1417-1425.
101. Roorda A, Metha AB, Lennie P, Williams DR. Packing arrangement of the three cone classes in primate retina. *Vision Res* 2001;41:1291-1306.